

Modeling of crack propagation in weak snowpack layers using the discrete element method

Johan Gaume¹, Alec van Herwijnen¹, Guillaume Chambon^{2,3}, Karl W. Birkeland⁴, and Jürg Schweizer¹

¹WSL Institute for Snow and Avalanche Research SLF, Davos, Switzerland

²Irstea, UR ETGR, Grenoble, France

³Université Grenoble Alpes, Grenoble, France

⁴USDA Forest Service National Avalanche Center, Bozeman, MT, USA

Correspondence to: Johan Gaume (gaume@slf.ch)

Abstract. Dry-snow slab avalanches are generally caused by a sequence of fracture processes including (1) failure initiation in a weak snow layer underlying a cohesive slab, (2) crack propagation within the weak layer and (3) tensile fracture through the slab which leads to its detachment. During the past decades, theoretical and experimental work has gradually led to a better understanding of the fracture process in snow involving the collapse of the structure in the weak layer during fracture. This now allows us to better model failure initiation and the onset of crack propagation, i.e. to estimate the critical length required for crack propagation. On the other hand, our understanding of dynamic crack propagation and fracture arrest propensity is still very limited. To shed more light on this issue, we performed numerical propagation saw test (PST) experiments applying the discrete element (DE) method and compared the numerical results with field measurements based on particle tracking. The goal is to investigate the influence of weak layer failure and the mechanical properties of the slab on crack propagation and fracture arrest propensity. Crack propagation speeds and distances before fracture arrest were derived from the DE simulations for different snowpack configurations and mechanical properties. Then, in order to compare the numerical and experimental results, the slab mechanical properties (Young's modulus and strength) which are not measured in the field, were derived from density. The simulations nicely reproduced the process of crack propagation observed in field PSTs. Finally, the mechanical processes at play were analysed in depth which led to suggestions for minimum column length in field PSTs.

1 Introduction

Dry-snow slab avalanches result from the failure of a weak snow layer underlying cohesive slab layers. The local damage in the weak layer develops into a crack which can expand if its size exceeds a critical length or if the load exceeds a critical value. Finally, crack propagation leads to the tensile fracture of the slab and ultimately, avalanche release (McClung, 1979; Schweizer et al., 2003). During the past decade, our understanding of the fracture process in snow has gradually evolved through the development of new theories as well as various field observations and experiments. The propagation saw test (PST), concurrently developed in Canada (van Herwijnen and Jamieson, 2005; Gauthier and Jamieson, 2006) and Switzerland (Sigrist and Schweizer, 2007), consists in isolating a snow column and initiating a crack of increasing length in the weak layer with a snow saw until the onset of rapid self-propagation of the crack. The PST allows observers to determine the critical crack length and evaluate crack propagation propensity. This field method has highlighted the importance of slab bending (due to the collapsible nature of weak snow layers) on crack propagation (e.g. van Herwijnen et al., 2010; van Herwijnen and Birkeland, 2014). On the other hand, theoretical and numerical models, based on fracture mechanics or strength of material approaches, were developed to investigate crack propagation and avalanche release (McClung, 1979; Chiaia et al., 2008; Heierli et al., 2008; Gaume et al., 2013, 2014b). While substantial progress has been made, application with regard to avalanche forecasting or hazard mapping is still hindered in part by our lack of understanding of the dynamic phase of crack propagation. For instance, based on practitioners' experience, it is not uncommon to perform PST field mea-

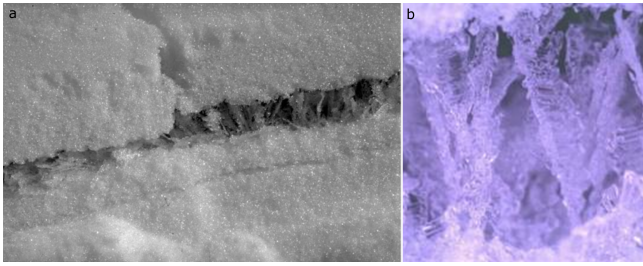


Figure 1: (a) Typical slab - weak layer configuration suitable for avalanche release. The weak layer is composed of surface hoar which is intact on the right and partially ruptured on the left. © ASARC from Jamieson and Schweizer (2000). (b) Zoom on a surface hoar crystal © ASARC.

surements with widespread crack propagation on one day, while a few days later, with seemingly very little changes in snowpack properties, cracks will no longer propagate (Gauthier and Jamieson, 2008). Thus far, there is no clear theoretical framework to interpret such observations, and it is not clear how and which snowpack properties affect dynamic crack propagation. This limitation is due to the complex microstructure of snow and its highly porous character (Fig. 1) which are not taken into account in the continuous approaches previously mentioned.

In this paper, numerical experiments of the propagation saw test (PST) are performed by applying the discrete element (DE) method which allows us to mimic the high porosity of snow. The goal is to investigate the influence of weak layer failure and the mechanical properties of the slab on crack propagation. In a first section, field data as well as the proposed model are presented. Then, crack propagation speed and distance before fracture arrest are derived from the DE simulations using the same method as for the field experiments (particle tracking). In a parametric analysis, we show the influence of single system parameters on the crack propagation speed and distance. Finally, the interdependence of snowpack properties is accounted for in order to compare numerical and experimental results and the mechanical processes leading to fracture arrest are analysed.

2 Data and methods

2.1 PST field data

Since the winter of 2004-2005, we collected data from 121 PST experiments at 46 different sites in Canada, USA and Switzerland (van Herwijnen and Jamieson, 2005; van Herwijnen and Heierli, 2009; van Herwijnen et al., 2010; Bair et al., 2012; van Herwijnen and Birkeland, 2014; Birkeland et al., 2014). At each site, we collected a manual snow profile and conducted one or several PSTs according to the procedure outlined in Greene et al. (2004). In many cases we

Gaume: Modeling of crack propagation

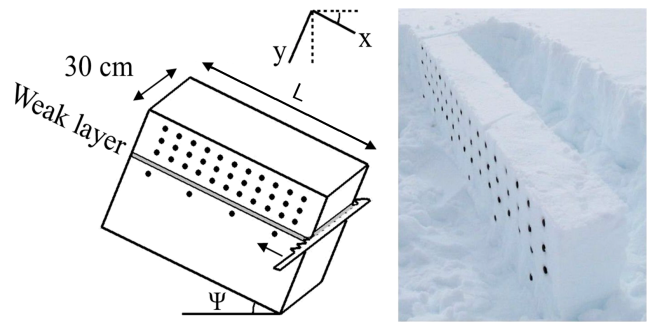


Figure 2: Schematic drawing and picture of the propagation saw test (PST). The black dots are markers used for particle tracking in order to measure the displacement of the slab. The column length is denoted L . Adapted from van Herwijnen et al. (2010).

used longer (than standard) columns to allow us to better investigate crack propagation. After columns preparation, we inserted black plastic markers into the pit wall and used a digital camera on a tripod to make a video recording of the PST (Fig. 2). We used a particle tracking velocimetry (PTV) algorithm to analyze the motion of the markers and thus the displacement of the snow slab above the weak layer (Crocker and Grier, 1996). In this way, the position of the markers in each video frame can be determined with a mean accuracy of 0.1 mm. The displacement of a marker is then defined as the movement relative to its initial position, that is, the average position of the marker prior to movement. For propagating cracks, there is a delay between the vertical displacement of subsequent markers. A typical displacement time-evolution for a propagating crack is shown in Fig. 3 for four slab markers. As explained in van Herwijnen and Jamieson (2005), the time delay between the onset of movement between markers is proportional to the distance between the markers and was used to calculate the propagation speed c of the fracture [see also Appendix A](#).

2.2 Discrete element model

2.2.1 Motivation and objectives

Discrete element (DE) modeling (Cundall and Strack, 1979) allows computing the motion of a large number of small grains by solving dynamic equations for each and defining a contact law between the grains. In addition, the DE method allows assessing mechanical quantities such as stress, displacement, deformation rate, porosity, etc. computed over representative elementary domains at each material point within the sample. Experimentally, this would be an impossible task. Hence, using DE, the mechanical and rheological behavior of the material can be explored locally, regardless of the spatial heterogeneities possibly displayed by the structure of the material and its mechanical quantities. This

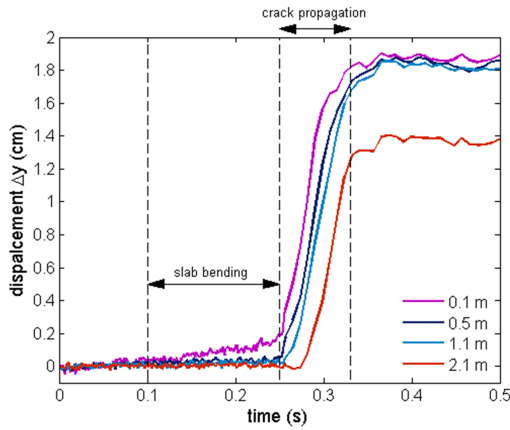


Figure 3: Temporal evolution of the measured vertical displacement Δy for a slab density of $\rho = 240 \text{ kg/m}^3$ obtained through PIV analysis of the marker's displacement from a field experiment. The different curves correspond to different horizontal positions in the slab, from the left-end ($x = 0.1 \text{ m}$) to the right-end ($x = 2.1 \text{ m}$).

method can thus help to better understand physical processes at play in granular assemblies. The DE method has been widely used to study the flow of granular materials within industrial (e.g. Chaudhuri et al., 2006; Sarkar and Wassgren, 2010) or environmental applications such as avalanche dynamics (e.g. Rognon et al., 2008; Faug et al., 2009). However, to our knowledge, discrete elements have never been used to model crack propagation in layered systems or to describe slab avalanche release processes. The latter processes are generally modeled under a continuum mechanics framework, using methods such as finite elements (Podolskiy et al., 2013, and references therein). These methods can be used to assess the stability of a layered snow cover, i.e. determine the conditions of failure occurrence and the onset of crack propagation. However, they are less suited to study what occurs after failure, i.e. during the dynamic phase of crack propagation, due to a lack in relevant constitutive models for the WL, including softening which induces a loss of objectivity with respect to the mesh in dynamic problems.

The objective of the proposed approach is to use the discrete element method (DE) to study the dynamic phase of crack propagation in a weak snowpack layer below a cohesive slab. The DE method is adequate for our purpose because: 1) no assumption needs to be made about where and how a crack forms and propagates, and 2) the model material is inherently discontinuous and well adapted to dynamic issues. We will show that, this method allows us to capture all the main physical processes involved in the release of dry-snow slab avalanches, namely the complex mechanical behavior of the weak layer and the interplay between basal crack propagation, slab bending, and slab fracture.

However, an important preliminary issue to address concerns the scale of the considered model. In the weak layer, we intend to represent, through a simplified description, the particular collapsible and highly porous micro-structure of the snow in order to be able to reproduce the main features of the failure envelope of this material. As will be shown, we achieve this by using triangular shapes of centimeter size. To account for the possible breakage of these elements, they consist of small cohesive grains of size r_{wl} . In the slab, on the contrary, due to computational costs, it would be completely unrealistic to try to account for the complete microstructure of the snow at the scale of a real slope or even at the scale of a field test such as the PST. The slab is thus modeled as a continuous material with an elastic-brittle constitutive behavior. Yet, similar to what is classically done for concrete (Meguro and Hakuno, 1989; Kusano et al., 1992; Camborde et al., 2000; Hentz et al., 2004), the response of this layer to the dynamic propagation of failure in the WL is also computed with the DE method. In that case, however, the considered elements (grains of size r) have no physical meaning and should only be regarded as entities of discretization similar to the mesh size in FE models. The contact parameters need to be properly calibrated (through classical biaxial tests, for instance) in order to recover the correct macroscopic properties of the material. Other continuous methods, such as FE, could have been used to simulate the slab, but – apart from avoiding the non-trivial issue of coupling DE and FE regions – the use of DE is well suited to represent the large deformations involved in the bending of the slab and the spontaneous formation of the tensile crack.

To summarize, we contend that, unlike in other DE applications which are at the scale of the microstructure (e.g. Cundall (1989); Iwashita and Oda (2000) for frictional granular materials or Hagenmuller et al. (2015) for snow), the grains involved in the DE model developed in this study should not be regarded as snow grains, and that both r_{wl} and r are only discretization scales whose choice will result from a compromise between resolution and computational cost as classically done to model concrete fracture (Hentz et al., 2004). We consider here a meter-scale model where the advantage of the DE method is its ability to mimic the poorly-known mechanical response of the weak layer and to account for the different modes of failure displayed by snow (shear, compression, tension). The only microstructural scale directly accounted for is the size of the triangular elements in the weak layer, which are on the same order as the weak layer thickness, since it is a necessary ingredient for reproducing the particular mechanical behavior of this layer.

2.2.2 Formulation of the model

Software The discrete element simulations were performed using the commercial software PFC2D (by Itasca), which implements the original soft-contact algorithm described in

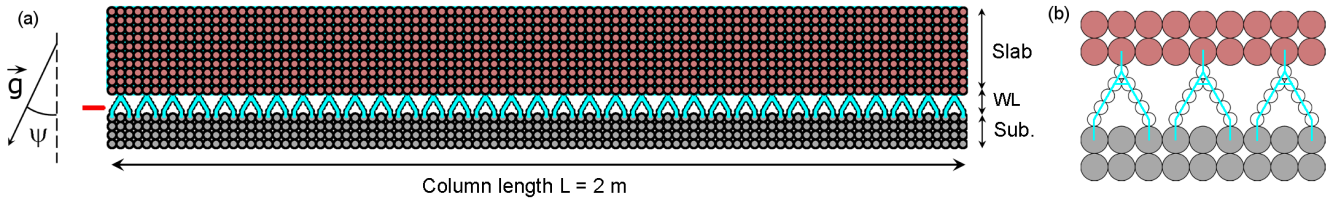


Figure 4: (a) Simulated system of the Propagation Saw Test (PST) composed of a slab, a weak layer and a rigid (fixed) substratum. The column is 2 m long. (b) Zoom on the weak layer structure. The blue lines represent the weak layer bonds.

k_n (N/m)	k_n/k_s	μ	e
1×10^4	2	0.5	0.1

Table 1: Mechanical parameters used in the simulations for the contact law. k_n : normal contact stiffness; k_s : tangential contact stiffness; μ : intergranular friction; e : normal restitution coefficient.

	\bar{k}_n (Pa/m)	\bar{k}_n/\bar{k}_s	σ_t (kPa)	σ_t/σ_s
slab	$1 \times 10^3 - 1.5 \times 10^6$	2	0-20	2
WL	8×10^5	2	0.6	2

Table 2: Mechanical parameters used in the simulations for the cohesive law. \bar{k}_n : bond normal stiffness; \bar{k}_s : bond shear stiffness. σ_t : macroscopic tensile strength; σ_s : macroscopic shear strength.

215 Cundall and Strack (1979).

Simulated system The simulated system (see Fig. 4a) is two dimensional and is composed of a completely rigid (fixed) basal layer, a WL of thickness D_{wl} and a slab of thickness D which were varied in the simulations. The slab is composed of grains of radius $r = 0.01$ m with a primitive square packing. The porosity of the slab is equal to 21%. Hence the density of the slab ρ can be adjusted by changing the grain density $\rho_{p,s}$ (varied in the simulations). The WL is composed of grains of radius $r_{wl} = r/2$ with a complex packing of collapsible triangular forms (see Fig. 4b) aimed at roughly representing the porous structure of persistent WLs such as surface hoar or depth hoar. The porosity of the WL is 70% and the density of the WL grains is $\rho_{p,wl} = 400$ kg/m³, leading to a WL density $\rho_{wl} = 120$ kg/m³. The length of the system (column length) is $L = 2$ m and the slope angle is denoted ψ . As mentioned above, the numerical grains are not intended to represent the real snow grains which are obviously smaller and have a different density. Nevertheless, as will be shown, this set up allows to capture the main features observed in field PSTs.

Loading The loading is applied by gravity and by advancing a ‘‘saw’’ (in red on Fig. 4a) at a constant velocity $v_{saw} = 2$ m/s through the weak layer. This saw is composed by rigid walls and has approximately the same thickness as field saws $h_{saw} = 2$ mm. The saw velocity was chosen relatively high to decrease the computational time, but lower than the lowest crack propagation speed observed in the field so as to correctly distinguish crack propagation from saw movement.

Contact law The cohesive contact law used in the simulations is the PFC parallel bond model represented schemati-

cally in Fig. 5a. The cohesive part acts in parallel to the classical linear contact law (Radjai et al., 2011; Gaume et al., 2011). For the linear component (in grey in Fig. 5a), the normal force is the sum of a linear elastic and of a viscous contribution (spring-dashpot model), and the tangential force is linear elastic with a Coulombian friction threshold. The corresponding mechanical parameters, namely the normal and shear stiffness k_n and k_s (elasticity parameters), the restitution coefficient e (viscous parameter) and the friction coefficient μ are summarized in Tab. 1. The value of the normal stiffness k_n was chosen in such a way that the normal interpenetration at contacts are kept small, i.e. to work in the quasi-rigid grain limit (da Cruz et al., 2005; Roux and Combe, 2002). Concerning the normal restitution coefficient e , we verified that the results presented below, and more generally all the macroscopic mechanical quantities obtained from the simulations, are actually independent of this parameter (in the range 0.1 - 0.9). This is due to the presence of the cohesive part of the contact law (see details below). Indeed, the restitution coefficient might have a strong influence for cases in which new contacts and collisions occur. In our case, the results are mostly driven by bond breaking which explains why e has no influence on the results.

The cohesive component (in black in Fig. 5a) can be envisioned as a point of glue with constant normal and shear stiffness \bar{k}_n and \bar{k}_s acting at the contact point. This bond has a specified shear and tensile strength σ_s^b and σ_t^b . The maximum tensile and shear stresses σ_{max} and τ_{max} at the bond periphery are calculated via beam theory according to:

$$\sigma_{max} = -\frac{F_n}{A} + \frac{||M||r_b}{I} \quad (1)$$

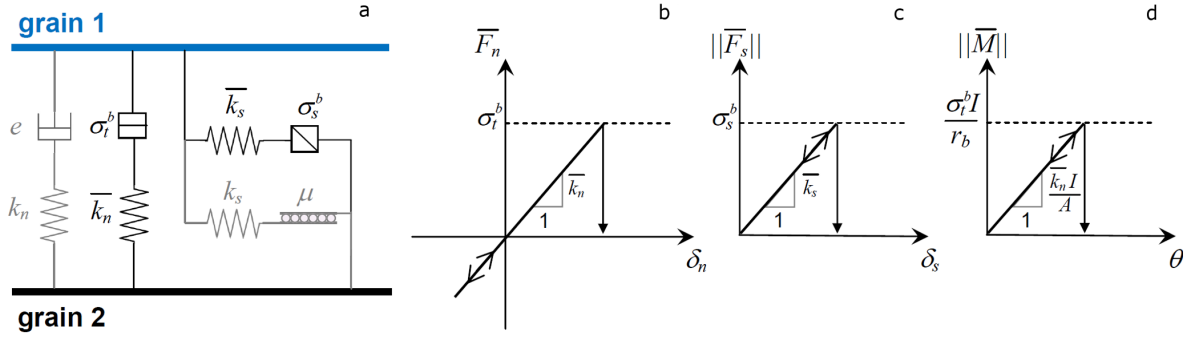


Figure 5: (a) Schematic representation of the parallel bond contact model which is used. The bonded part is represented in black while the unbonded part is represented in grey. (b) Bond normal force \overline{F}_n as a function of normal interpenetration δ_n between two grains. (c) Bond shear force $||\overline{F}_s||$ as a function of tangential interpenetration δ_s between two grains. (d) Bond bending moment $||\overline{M}||$ as a function of bending rotation θ between two grains.

$$\tau_{max} = \frac{||\overline{F}_s||}{A} \quad (2)$$

where F_n and F_s are the bond normal and shear forces, M is the bending moment, r_b the bond radius, $A = \pi r_b^2$ the bond area and $I = \pi r_b^4/4$ its moment of inertia. If the tensile stress exceeds the bond tensile strength, the bond breaks and both the normal and shear contact forces are set to zero (Fig. 5b). If the shear stress exceeds the bond shear strength, the bond also breaks (Fig. 5c) but the contact forces are not altered, provided that the shear force does not exceed the friction limit, and provided that the normal force is compressive. The bond can also break if the bending moment exceeds $\sigma_t^b I/r_b$ (Fig. 5d). The ranges of parameters used for the bond model are summarized in Tab. 2.

As the two components are acting in parallel, the total stiffness of the bonded contact is equal to the sum of the contact stiffness k_n and the bond stiffness \overline{k}_n :

$$k_{tot} = k_n + \overline{k}_n. \quad (3)$$

Finally, in our case of a square grain assembly, the Young's modulus can be derived analytically from k_n and \overline{k}_n according to:

$$E = \frac{1}{\pi r_b} (k_n + \overline{k}_n). \quad (4)$$

The contact stiffness k_n was kept constant at 1×10^4 N/m and \overline{k}_n was varied between 1×10^3 and 1.5×10^6 N/m (for the slab) leading to realistic values of the Young's modulus E between 0.35 and 50 MPa. It was verified from biaxial tests that the macroscopic (bulk) Young's modulus of the slab effectively follows this relationship due to the specific (squared) structure of the slab.

Time step and elastic waves The time step was computed classically as a function of the grain properties according to

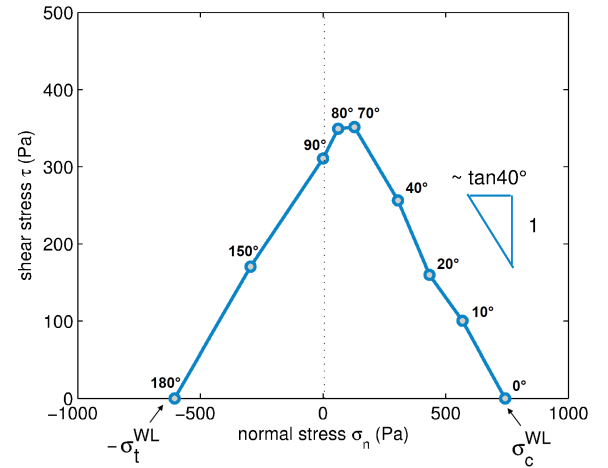


Figure 6: Failure envelope of the modelled WL obtained from mixed-mode shear-compression loading tests. The angle represented next to the data points is the slope angle, σ_t^{WL} and σ_c^{WL} are the tensile and compressive strengths, respectively.

$\Delta t = \sqrt{m/k} \approx r \sqrt{\rho/E}$ where m , ρ and r are the smallest grain mass, density and radius and k and E the largest contact/bond stiffness and Young's modulus, respectively. The choice of this time-step insures the stability of the algorithm and that the crack propagation speed is lower than the speed of the elastic waves in the sample. The order of magnitude of the speed of elastic waves in the sample is $c^e \approx \sqrt{E/\rho}$.

2.2.3 Simulation protocol and illustration

First, the macroscopic properties of the slab have to be determined as a function of the microscopic properties of the bond. For the slab, bi-axial tests were carried out which allowed to validate that for a squared assembly, the macro-

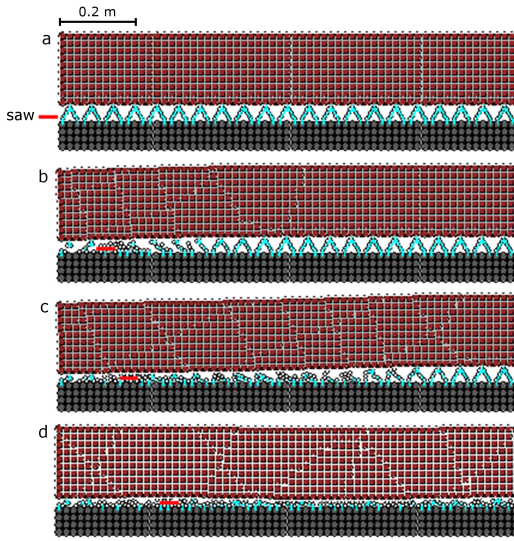


Figure 7: Snapshots of a PST numerical experiment. (a) Initial system $t = 0.1$ s, (b) onset of crack propagation $t = 0.26$ s, (c) dynamic propagation $t = 0.28$ s; (d) complete failure of the WL $t = 0.45$ s.

scopic (bulk) Young's modulus depends on bond stiffness according to Eq. (4).

325 For the weak layer, similarly, simple loading tests were carried out to compute the macroscopic failure criterion (mixed mode shear-compression) of the WL as a function of the bonds of WL grains (Gaume et al., 2014a). The failure envelope of the WL is strongly anisotropic as shown in Fig. 6. This failure envelope shows, for realistic values of the slope angle, a much lower strength in shear than in compression as well as a decrease of the shear strength with increasing normal stress. This type of behaviour is similar to that reported in recent laboratory (Reiweger et al., 2015) and field (Chandel et al., 2014) experiments on persistent weak snow layers. Hence, the chosen WL structure allows to have different modes of failure (tension, shear, compression and mixed-mode) such as observed in real weak layers and thus has the essential characteristics to model the processes of slab avalanche release.

340 Then, PST simulations were performed. An illustration of a simulation result highlighting the displacement wave of the slab is shown in Fig. 7 and the associated vertical displacement Δy is represented in Fig. 8. The critical length is denoted a_c and corresponds to the translation length of the saw required to obtain a self-propagating crack.

345 In order to determine the crack propagation speed, purely elastic simulations (infinite tensile and shear strength of the bonds between slab grains) were carried out. The propagation speed was computed using the same method as for field PSTs by analyzing the vertical displacement wave of the slab (van Herwijnen and Jamieson, 2005). This procedure is presented in more detail in Appendix A.

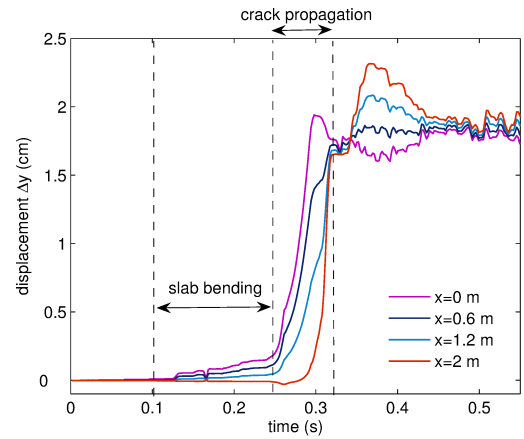


Figure 8: Temporal evolution of the modeled vertical displacement Δy of the slab for a slab density $\rho = 250$ kg/m^3 . The different curves correspond to different horizontal initial positions of the slab, from the left-end ($x = 0$ m) to the right-end ($x = 2$ m).

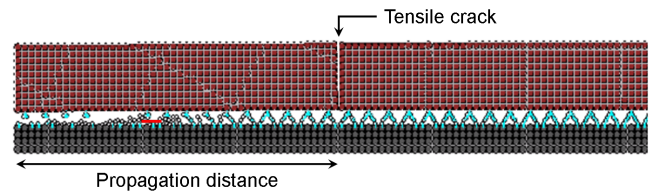


Figure 9: Snapshot of a PST with fracture arrest due to tensile crack opening in the slab induced by slab bending.

The propagation distance was computed by taking into account the possible failure of the slab by setting finite values to the tensile and shear strength of the slab (σ_t , σ_s). We define the propagation distance as the distance between the left wall of the system and the location where the tensile crack opens at the slab surface, as shown in Fig. 9. This measure of the propagation distance differs from that defined by Gauthier and Jamieson (2006) who defined it as the distance between the point of onset of crack propagation in the WL and the point of slab failure. However, we argue that the propagation distance, as we define it, is a more suitable measure since this is the one that influences the stresses in the slab and thus fracture arrest propensity. Similarly, for a real avalanche, the important distance for the bending induced stress and for the avalanche release size is the distance from the very first failure initiation point (whatever the nature of the initial trigger), to the location of the slab tensile failure, and not from the crack tip at the moment of the onset of crack propagation.

For the parametric analysis (Sec. 3.2), we performed simulations for which only one system parameter was modified while the other parameters were kept constant. The parameters used are described in Tab. 3. However to apply these results to slab avalanche release and in order to compare our re-

sults to field data (Sec. 3.3), existing relations between snow-pack properties were taken into account. Hence, simulations were performed for different slab densities with the Young's modulus varying according to an empirical exponential fit to the data reported by Scapozza (2004):

$$E = 1.873 \times 10^5 e^{0.0149\rho}, \quad (5)$$

and with a tensile strength varying according to a power-law fit to the data reported by Sigrist (2006):

$$\sigma_t = 2.4 \times 10^5 \left(\frac{\rho}{\rho_{ice}} \right)^{2.44} \quad (6)$$

with $\rho_{ice} = 917 \text{ kg/m}^3$.

3 Results

3.1 Displacement of the slab

The evolution of the vertical displacement Δy of the slab is represented in Fig. 8. In this figure together with the illustration of the displacement wave of the slab (Fig. 7), one can clearly observe the different processes acting before, during and after crack propagation. First, slab bending occurs prior to the onset of crack propagation and the dynamic propagation phase. These distinct phases (stable bending of the slab and crack propagation) are also clearly visible in the vertical displacement Δy , as shown in Fig. 8 for four different horizontal positions in the slab.

Between 0 and 0.1 s nothing happens, then as the saw advances, the vertical displacement slowly increases. This phase corresponds to the bending of the under-cut part of the slab. Then, for $t = 0.25$ s approximately, the critical length a_c was reached and the displacement increases abruptly, even beyond the saw, corresponding to the dynamic crack propagation phase. After $t = 0.3$ s, the slab has reached the broken WL at the left-end of the slab for $x = 0$ m. After 0.32 s, the entire WL has collapsed leading to a constant vertical displacement of the slab approximately equal to $\Delta y = 1.8$ cm. This displacement is not perfectly equal to the WL thickness because of the grains remaining in the WL. The peak in the displacement around $t = 0.38$ s is an artefact associated with the movement of the saw after the crack has propagated which does not affect the results that we will present.

3.2 Parametric analysis

3.2.1 Crack propagation speed

For all the simulations carried out, the crack propagation speed varied between 5 and 60 m/s. Fig. 10a shows that the crack propagation speed c strongly increases with the Young's modulus E of the slab, from less than 5 m/s for very soft slabs ($E < 1$ MPa) to 40 m/s for an almost rigid

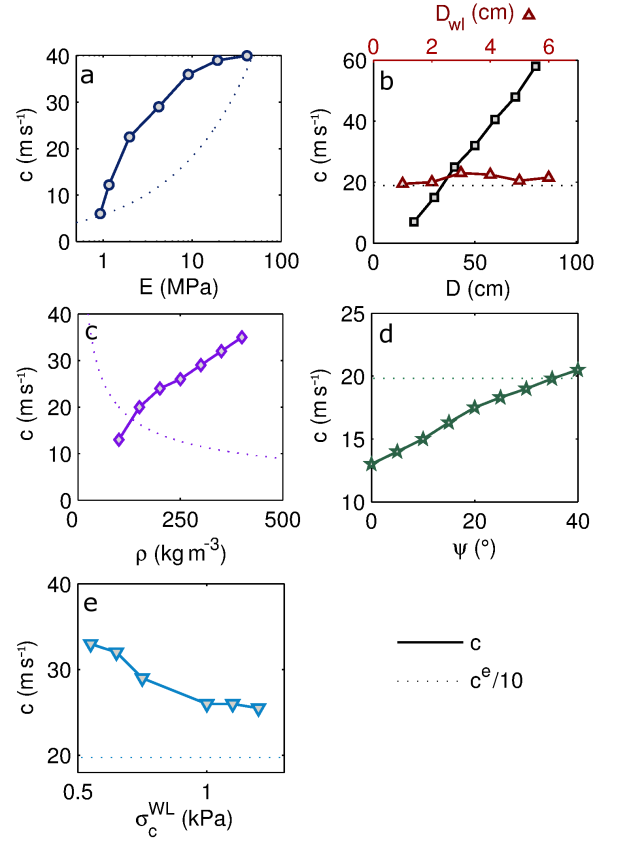


Figure 10: Crack propagation speed c (continuous lines) and speed of elastic waves in the slab $c^e/10$ (dotted lines) as a function of (a) the Young's modulus of the slab E , (b) slab thickness D and WL thickness D_{wl} , (c) slab density ρ , (d) slope angle ψ and (e) WL compressive strength σ_c^{WL} . The parameters used for these figures are given in Tab. 3.

slab ($E \approx 50$ MPa) where the increase levels off. The propagation speed c also strongly and linearly increases with the thickness of the slab D (Fig. 10b), from almost zero for a slab thickness lower than 10 cm to 60 m/s for a thickness of 80 cm. Similar, to the thickness, the propagation speed increases almost linearly with the density of the slab ρ (Fig. 10c) and the slope angle ψ (Fig. 10d). The propagation speed seems not to be influenced by the thickness of the WL (Fig. 10b) as soon as the failure occurs under the same conditions (same critical length). Furthermore, the propagation speed decreases with increasing WL strength (Fig. 10e). This suggests that the crack propagation speed is mostly influenced by the failure conditions (load due to the slab and WL strength) rather than structural parameters such as the WL thickness.

Finally, the speed of the elastic waves in the slab (c^e) is always substantially higher than the crack propagation speed (approximately 10 times lower, Fig. 10). In addition, we can observe that the speed of the elastic waves in the slab is not

	ρ	E	σ_t^{slab}	D	D_{wl}	ψ	σ_c^{WL}
Fig. 10a	300 kg/m ³	-	Inf.	20 cm	4 cm	0°	750 Pa
Fig. 10b	100 kg/m ³	4 MPa	Inf.	- / 20 cm	4 cm / -	0°	750 Pa / *
Fig. 10c	-	4 MPa	Inf.	20 cm	4 cm	0°	750 Pa
Fig. 10d	100 kg/m ³	4 MPa	Inf.	20 cm	4 cm	-	750 Pa
Fig. 10e	300 kg/m ³	4 MPa	Inf.	20 cm	4 cm	0°	-
Fig. 11a	300 kg/m ³	-	-	20 cm	4 cm	0°	750 Pa
Fig. 11b	300 kg/m ³	4 MPa	-	20 cm	-	0°	*
Fig. 11c	150 kg/m ³	4 MPa	-	20 cm	4 cm	-	750 Pa
Fig. 11d	-	4 MPa	2 kPa	20 cm	4 cm	0°	750 Pa
Fig. 11e	100 kg/m ³	4 MPa	1.5 kPa	-	4 cm	0°	750 Pa
Fig. 11f	300 kg/m ³	4 MPa	2 kPa	-	4 cm	0°	-

Table 3: Table of the parameter values used for Figs. 10 and 11. The symbol ‘-’ means that the associated parameter was varied. The symbol * means that the WL failure envelope was calibrated to obtain a constant critical length $a_c = 15$ cm.

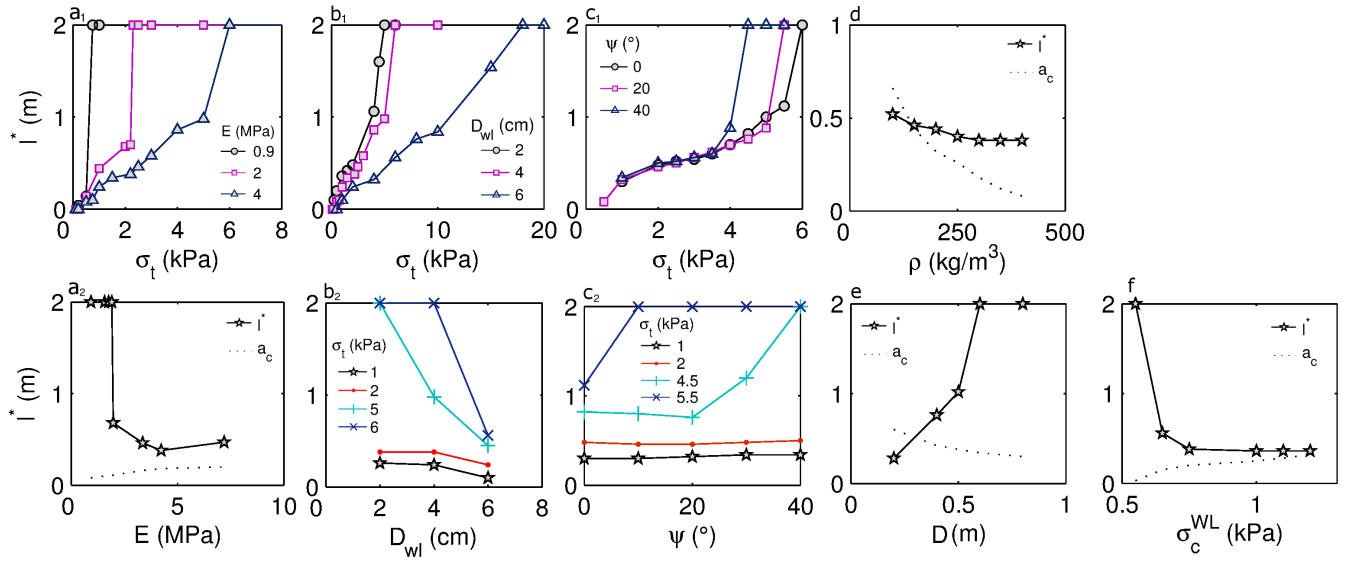


Figure 11: Crack propagation distance l^* as a function of the tensile strength σ_t and the Young’s modulus E of the slab (a_1 - a_2), the tensile strength σ_t and the WL thickness D_{wl} (b_1 - b_2), the tensile strength σ_t and the slope angle ψ (c_1 - c_2), slab density ρ (d), slab thickness D (e) and WL compressive strength σ_c^{WL} (f). a_c denotes the critical cut length for crack propagation. The parameters used for these plots are given in Tab. 3.

440 a good proxy to explain the trends in the crack propagation
 445 speed as shown for instance by the opposite trends with density
 450 (Fig. 10c).

3.2.2 Propagation distance

445 Fig. 11 shows propagation distance as a function of different
 450 system parameters. Figs. 11a₁, 11b₁ and 11c₁ show the
 460 increase of the propagation distance with increasing tensile
 465 strength of the slab σ_t . This result was expected since a
 470 stronger slab requires a larger tensile stress in order to break
 475 and thus a larger propagation distance is required to obtain
 480 sufficient tensile stresses in the slab (induced by bending or
 485 by the shear component of the the slab’s weight additionally
 490 in case of $\psi \neq 0$).

445 The influence of the Young’s modulus E of the slab is
 450 shown in Figs. 11a₁ and 11a₂. Overall, propagation distance
 455 decreases with increasing Young’s modulus. Hence, the
 460 softer the slab is, the lower is the fracture arrest propensity.
 465 For a tensile strength of 2 kPa (Fig. 11a₂), the propagation
 470 distance l^* sharply decreases from 2 m (column length) to
 475 an approximately constant value $l^* = 0.5$ m for $E \approx 2$ MPa.
 480 Also, Fig. 11a₁ shows that for higher Young’s modulus,
 485 larger tensile strength values are required to obtain full
 490 propagation. The critical length a_c for crack propagation was
 495 also represented in Fig. 11a₂ to show that the tensile failure
 500 across the slab always occurred (in this case) after the onset
 505 of crack propagation.

Then, the influence of WL thickness D_{wl} is shown in
 Figs. 11b₁ and 11b₂. The WLs have different thickness but

the same failure criterion and thus the same critical length a_c which is equal to 15 cm in this case. The propagation distance l^* decreases with increasing WL thickness. For low values of the tensile strength of the slab, the propagation distance is small and almost independent of the WL thickness whereas an important decrease is observed for larger values of the tensile strength. In other words, thicker weak layers result in more slab bending so that slab failure becomes more likely due to high tensile (bending) stress.

Figs. 11c₁ and 11c₂ show the influence of slope angle ψ on propagation distance. Similarly to WL thickness, slope angle seems to have no influence on the propagation distance for low values of the tensile strength. However, for larger values of σ_t ($\sigma_t > 4$ kPa), the propagation distance strongly increases with increasing slope angle ψ . Hence, fracture arrest propensity decreases with slope angle for large values of the tensile strength of the slab, typically higher than 4 kPa. This result is not trivial, since as the slope angle increases, there is a competition between the decreasing slab bending which results in a decrease of the tensile stresses in the slab and an increase of the tensile stresses due to the weight of the slab in the slope parallel direction. Hence, this result suggests that slab bending is the primary process influencing tensile failure of the slab (for homogeneous properties of the system).

Crack propagation distance slightly decreases with slab density as shown in Fig. 11d. For very low slab densities, the critical length a_c is relatively high and thus the tensile failure across the slab occurs before the critical length is reached. Then, as the density of the slab increases, the critical length decreases and the propagation distance stabilizes around 0.4 m.

Whereas slab density ρ and slab thickness D have a similar influence on the stability of the system, on the crack propagation speed (Figs. 10b and 10c) and on the onset of crack propagation, as suggested by the decrease of the critical length a_c with both ρ and D (Figs. 11d and 11e), their influence on fracture arrest propensity differs. Indeed, in contrast to the influence of slab density, the propagation distance strongly increases with increasing slab thickness (Fig. 11e). Hence, the thicker the slab is, the lower is the fracture arrest propensity. This results can be easily explained using beam theory (Timoshenko and Goodier, 1970) to express the maximum tensile stress in a bending slab which is inversely proportional to the slab thickness D (see Sec. 3.4 or Schweizer et al., 2014).

Finally, crack propagation distance decreases with WL strength (Fig. 11f) for low WL strength values for which the system is close to the overall failure (the critical length is close to zero). However, for higher values of the WL strength, the propagation distance is almost unaffected by this property of the WL.

3.3 Comparison with field data

The results of the previous parametric analysis should be interpreted with care since for snow, several of the system pa-

ρ (kg/m ³)	100	150	200	250	300
D (cm)	30	40	50	65	80

Table 4: Average slab thickness as a function of slab density for PST field data.

rameters are inter-related leading to more complex interactions. For instance, the result about the influence of Young's modulus on the propagation distance might seem contradictory to avalanche observations. Indeed, taken as it is, this result would imply that it is easier to trigger a tensile failure in stiff and thus hard snow than in soft snow. Consequently, harder slabs would result in smaller release areas than soft slabs which is clearly in contradiction with avalanche observations (van Herwijnen and Jamieson, 2007). Hence, even if the result behind Fig. 11a₂ is consistent, from a mechanical point of view, it cannot be directly applied to dry-snow slab avalanche release. To do so, one should take into account the relations between slab density ρ , Young's modulus E and tensile strength σ_t according to Eqs. (3) and (4). Simulations were performed for slab densities ranging from 100 to 300 kg/m³, corresponding to a Young's modulus E of the slab between 0.8 and 16 MPa [Eq. (3)] and a tensile strength σ_t between 1 and 16 kPa [Eq.(4)].

In order to compare our numerical model to PST field data, we selected two simulation cases to show the overall trend of the propagation speed and distance with density, rather than simulating precisely each of the PSTs individually (which are prone to some variability) by using the available initial conditions from the field.

In the following, we distinguish two simulation cases:

- **Case #1** corresponds to simulations with a constant slab thickness $D = 20$ cm, slope angle $\psi = 0^\circ$ and WL properties ($\sigma_c^{\text{WL}} = 750$ Pa);
- **Case #2** corresponds to a case with a slope angle $\psi = 23^\circ$ which is the average slope angle of our field PSTs and a slab thickness D which is also a function of density according to field data (Tab. 4). In addition, we calibrated the strength of the WL bonds in order to have the same critical length for the different densities. This ensured we observed crack propagation and avoid the global and simultaneous failure of the entire WL. Indeed, as density increases, the critical length a_c decreases and tends to zero (Fig. 11d) leading to the instability of the system without cutting the WL.

A similar choice was made by Gaume et al. (2015) who computed the tensile failure probability for two cases (constant depth or constant load) with similar trends in the results.

3.3.1 Displacement of the slab

Our numerical results (Fig. 8) obtained for a slab density $\rho = 250$ kg/m³ are in very good agreement with experimental re-

sults (Fig. 3) obtained for a similar density of $\rho = 240 \text{ kg/m}^3$. Indeed, the same phases in the displacement curves, corresponding to slab bending and crack propagation, were observed in the measurements. Furthermore, the amount of slope normal displacement prior to crack propagation as well as the fracture time, defined as the time it takes for the slab to come into contact with the broken weak layer, were very similar. Finally, we would like to point out that the total slope normal displacement after crack propagation in our experimental results was not the same for all markers (Fig. 3), which has often been observed in previous studies (van Herwijnen et al., 2010; Bair et al., 2014), whereas it is approximately the same in the numerical simulations if no fracture arrest occurred (Fig. 8). This difference is presumably due to 3D and edge effects such as wall friction at the right side of the column.

3.3.2 Crack propagation speed

The crack propagation speed c obtained in field PSTs and from the simulated PSTs is represented as a function of slab density in Fig. 12. Overall, the propagation speed obtained from field PSTs increases from 10 to 50 m/s as the density of the slab increased from 140 to 300 kg/m^3 . The gray squares represent the cases with fracture arrest due to tensile fracture of the slab (SF) for which the crack propagation speed is not very accurate and generally lower than the velocity measured when the slab did not break (END: open squares for full propagation).

Overall, both simulation cases #1 and #2 reproduce the magnitude of the propagation speed c and the increasing trend with increasing slab density ρ . The case #2 model (relation between slab density, Young's modulus, thickness and slope angle) slightly overestimates the average propagation speed but provides good estimates for densities higher than 250 kg/m^3 . Furthermore, the simulations of case #2 were done for the same conditions of failure initiation, i.e. the strength of the WL bonds was calibrated in order to have the same critical length for the different densities. However, for the experiments, the critical length generally increases with increasing density due to the settlement which induces an increase of Young's modulus and a strengthening of the WL (Zeidler and Jamieson, 2006a, b; Szabo and Schneebeil, 2007; Podolskiy et al., 2014). In contrast, for case #1, a decrease in slab thickness and slope angle induces a decrease in the crack propagation speed (Fig. 10), explaining why the speeds for case #1 ($\psi = 0^\circ$ and $D = 20 \text{ cm}$) are lower. In addition, for case #1, the WL properties were kept constant, which together with the increase of the Young's modulus (less bending) with density resulted in an increase of the critical length with density. This is in agreement with field observations which might explain the better quantitative agreement with the experiments.

Finally, for a low slab density $\rho = 100 \text{ kg/m}^3$ ($E = 0.83 \text{ MPa}$), the speed of the elastic waves in the slab c^e is about

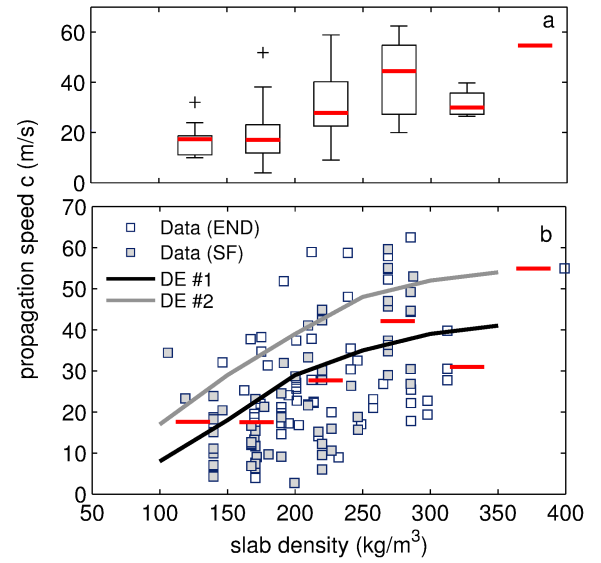


Figure 12: (a) Boxplot of the propagation speed c versus slab density for all field experiments. The data were grouped by slab density classes of 50 kg/m^3 . The red line represents the median value, the edges of the box are the 25th and 75th percentiles, the whiskers extend to the most extreme data points without considering the outliers, and outliers are plotted individually as a cross. (b) Crack propagation speed c vs slab density ρ . The open squares correspond to field PSTs with full propagation (END) and the solid squares correspond to PSTs with fracture arrest (SF). The black line corresponds to the result of the DE model taking into account the relation between slab density, Young's modulus for a slope angle $\psi = 0^\circ$ and a slab thickness $D = 20 \text{ cm}$ (case #1). The gray continuous line corresponds to the result of the DE model taking into account the relation between slab density, Young's modulus and thickness for a slope angle $\psi = 23^\circ$ (case #2). The red lines represent the median values of the density classes (same as in (a)). The data consist of $N=121$ PST experiments.

90 m/s, whereas the crack propagation speed is around 15 m/s. For a high density $\rho = 300 \text{ kg/m}^3$ ($E = 16 \text{ MPa}$), $c^e \approx 230 \text{ m/s}$, whereas the crack propagation speed is around 45 m/s.

3.3.3 Propagation distance

The proportion between the number of experiments for which fracture arrest was observed N_{SF} and the total number of experiments $N_{SF} + N_{END}$ decreases with increasing slab density ρ (Fig. 13a). This figure highlights the important decrease of fracture arrest propensity with slab density. For slab densities higher than 300 kg/m^3 the number of experiments with slab fracture is very small ($N_{SF} < 20\%$).

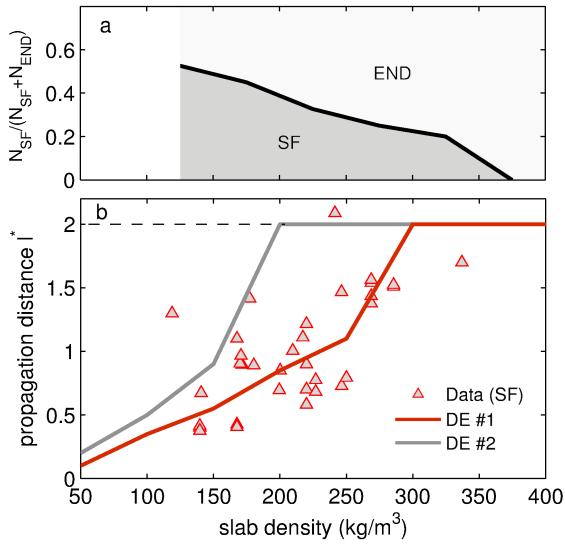


Figure 13: (a) Proportion between the number of experiments with slab fracture N_{SF} and the total number of experiments $N_{SF} + N_{END}$ for different classes of density. (b) Propagation distance l^* vs slab density ρ only for cases with fracture arrest (SF). The red line corresponds to case #1 and the gray line corresponds to the column length $L = 2$ m in the PST simulations.

The crack propagation distance l^* is represented as a function of slab density in Fig. 13b. Only cases with slab fracture (SF) were represented. Overall, the propagation distance obtained from field PSTs increased with slab density and varies approximately from 0.4 to 2.1 m as the density increased from 140 to 300 kg/m^3 . This trend is well reproduced by the discrete element simulations for both cases, but with a better qualitative agreement for case #1. For case #1 and for densities higher than about 300 kg/m^3 , no fracture arrest is observed resulting in full propagation of the crack in the WL over the entire column length (END). For case #2, this transition occurs already for a density of about 200 kg/m^3 . Besides, we would like to point out that field PSTs were not made systematically for the same column lengths. However, we checked numerically that, as soon as fracture arrest occurs within the column, the crack propagation distance is almost independent of the column length. For instance, if a propagation distance of 0.7 m is observed for a column length of 1.5 m, it will be the same for a column of 2.5 m. This is true as soon as the column length is higher than the length over which edge effect are observed (length typically lower than 1 m, Gaume et al., 2013).

The experiments and the simulations confirm that dense and hard snow slabs are more prone to wide-spread crack propagation than soft slabs.

3.4 Mechanical processes of fracture arrest

In order to better understand the underlying mechanical processes of fracture arrest in the slab, the normal stresses in the slab σ_{xx} have to be compared with its tensile strength σ_t . The normal stresses in the slab were computed for each grain from contact forces using the classic Love homogenization formula (Cambou and Jean, 2001). A tensile crack in the slab occurs when the maximum normal stress σ_{xx}^m exceeds the tensile strength. Hence, we analyzed the evolution of normal stresses in the slab during the process of crack propagation for case #1 with a slab density $\rho = 250 \text{ kg/m}^3$ leading to a tensile strength $\sigma_t = 10 \text{ kPa}$ [Eq. (4)]. First, before the onset of crack propagation, an increase of tensile stress occurs at the top of the slab close to the crack tip of the WL (Fig. 14). The bottom of the slab is subjected to an increase in compression ($\sigma_{xx} < 0$). This increase of tensile stress is due to the bending of the slab and increases with increasing crack length (Timoshenko and Goodier, 1970).

Then, once the critical length is reached, the crack becomes self-propagating. The crack length increase leads to an increase of the tensile stresses in the slab. Note that the maximum tensile stress σ_{xx}^m is always located at the top surface of the slab, not directly at the vertical of the crack tip but slightly shifted to the right above the undamaged weak layer (Fig. 14). At one point the maximum tensile stress meets the tensile strength of the slab ($\sigma_t = 10 \text{ kPa}$) which leads to the opening of a tensile crack and fracture arrest. This fracture arrest leads to the unloading of the slab where the stresses become close to zero everywhere, except at the position of the saw where some small local bending effects still occur.

In order to better understand why fracture arrest does not occur anymore for high densities, as shown in Fig. 13, we then analyzed the maximum tensile stress σ_{xx}^m as a function of slab density in the case of a purely elastic slab for which the Young's modulus was varied according to Eq. (3) (case #1). The DE results were then compared to those predicted by the static beam theory. According to beam theory (Timoshenko and Goodier, 1970), the maximum theoretical tensile stress in a beam of length l , thickness D embedded on its right side and subjected to gravity, with an angle ψ (with regards to the horizontal) is equal to

$$\sigma_{xx}^{th} = \rho g l \sin \psi + \frac{3 \rho g \cos \psi l^2}{D}. \quad (7)$$

As we have seen before in Fig. 14, the tensile stress in the slab increases during propagation due to an increase of the crack length. However, this length is limited by the amplitude of collapse h_c of the WL (Fig. 15a). Indeed, once the left part of the slab comes into contact with the broken WL, the tensile stress reaches a maximum value and does not increase anymore (see also Fig. 7c). The length l_0 (already introduced by Heierli et al., 2008) required to come into contact with the broken WL can be obtained analytically by computing the

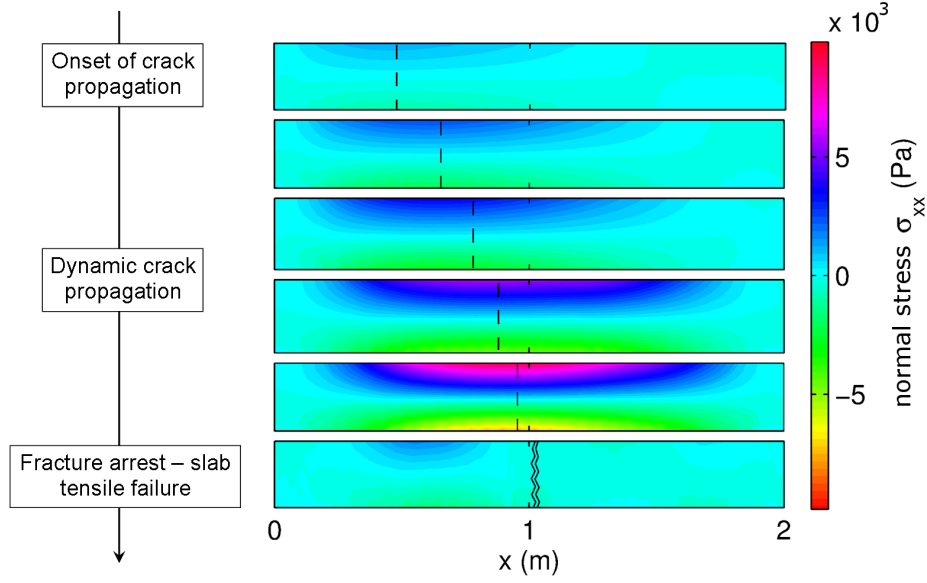


Figure 14: Evolution of the normal stress σ_{xx} in the slab during the process of crack propagation for a case #1 simulation and a density of 250 kg/m^3 with a tensile strength of 10 kPa. The normal stress σ_{xx} was calculated for each grain from contact forces according the Love homogenization formula and linearly interpolated between grains. The dashed lines represent the position of the crack tip in the WL.

vertical displacement of the slab according to beam theory and is equal to

$$l_0 = \left(\frac{2ED^2h_c}{3\rho g \cos\psi} \right)^{1/4}. \quad (8)$$

Hence, the overall maximum theoretical tensile stress $\sigma_{xx}^{m,th} = \sigma_{xx}^{th}(l_0)$ is found by replacing l by l_0 in Eq. (7).

For low values of slab density ($\rho < 175 \text{ kg/m}^3$, Fig. 15b), the maximum tensile stress increases with increasing density and the DE model results are very well reproduced by beam theory. In addition, the maximum tensile stress is always higher than the tensile strength of the slab, leading to systematic fracture arrest for these low density values. However, for higher densities, beam theory predicts a strong increase of the maximum tensile stress with density, so that the stress would always be higher than the tensile strength of the slab. This would lead to systematic fracture arrest for any value of the density which is in contrast to the results of both field and numerical PSTs. The DE model results, in particular, show that for a slab density higher than about a threshold density $\rho' = 180 \text{ kg/m}^3$, the maximum tensile stress starts to decrease with increasing density. Ultimately, for a density of approximately 280 kg/m^3 , the maximum tensile stress becomes lower than the strength, leading to full propagation of the crack in the WL, in agreement with Fig. 13 (case #1).

This result highlights the limits of the static beam theory and thus the need to take into account dynamic effects when addressing fracture arrest propensity issues. Indeed, we sup-

pose that the reason of this sudden decrease is due to the crack propagation speed which becomes higher as slab density increases and induces a loss of support in the slab where stresses do not have time to establish. In other words, the displacement of the slab due to gravity is too slow to establish a mechanical equilibrium between bending and gravity. For instance, if we assume that the crack would propagate at an infinite speed, then the tensile stresses in the slab would not increase after reaching the critical length. The maximum tensile stress in the slab would thus be the one obtained at the moment of the onset of crack propagation. Obviously, the propagation speed is not infinite but limits the establishment of the stresses in the slab.

Using the theoretical relationships for $\rho < \rho'$ ($\sigma_{xx}^m = \sigma_{xx}^{th}$) and an empirical (exponential) fit to the data for $\rho > \rho'$ ($\sigma_{xx}^m = \sigma_{xx}^{dyn}$), one can compute the theoretical propagation distance l_{th}^* by solving

$$\sigma_{xx}^m(l_{th}^*) = \sigma_t. \quad (9)$$

The theoretical propagation distance l_{th}^* was represented in Fig. 15c for both zones ($l_{th}^* = l_{bt}^*$ for $\rho < \rho'$ and $l_{th}^* = l_{dyn}^*$ for $\rho > \rho'$) as well as the characteristic distance l_0 . Again the beam theory reproduces the results for low densities well. For these low densities, the tensile failure in the slab occurs even before the onset of crack propagation due to the low value of the associated tensile strength. However, the important increase of the propagation distance for densities higher than ρ' is not reproduced by beam theory. On the other hand, using the empirical relation (exponential fit of the maximum ten-

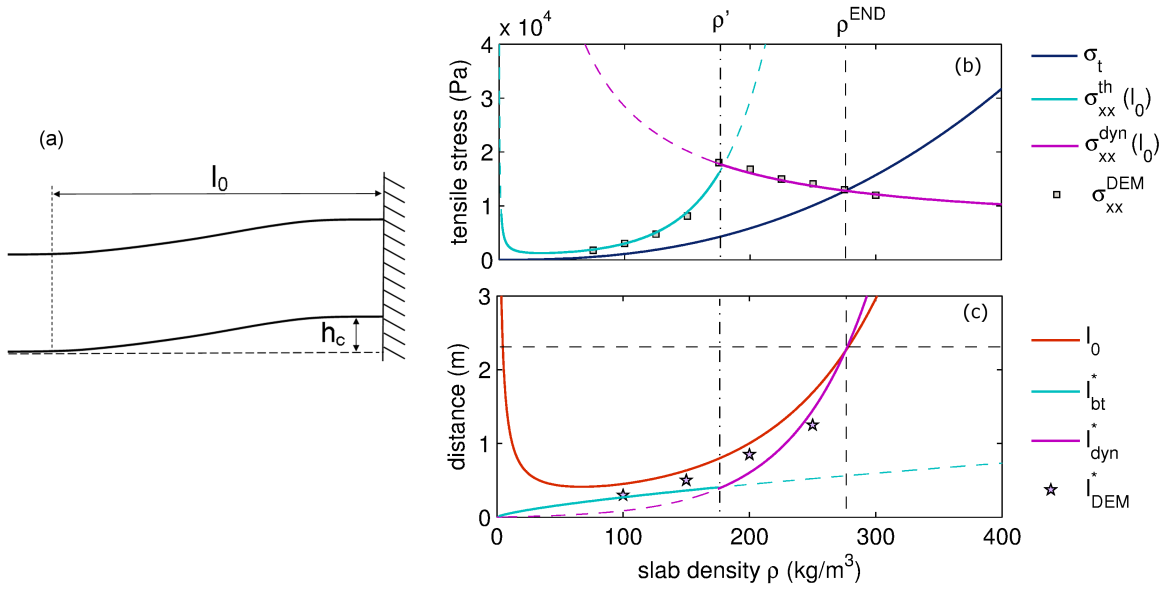


Figure 15: (a) Illustration of the characteristic length l_0 required for the slab to be in contact with the broken WL. h_c represents the collapse height. (b) Maximum tensile stress σ_{xx}^m as a function of slab density for the discrete element model σ_{xx}^{DEM} , with a purely elastic slab and case #1, according to beam theory $\sigma_{xx}^{th}(l_0)$ and from an empirical (exponential) fit $\sigma_{xx}^{dyn}(l_0)$. The tensile strength of the slab σ_t is also represented as a function of slab density σ_t . (c) Propagation distance for the same cases as in (b) plus l_0 as a function of slab density.

sile stress in Fig. 15b), the strong increase of the propagation distance is well reproduced. After a certain value of the density $\rho^{END} = 280 \text{ kg/m}^3$, the propagation distance l_{dyn}^* becomes higher than l_0 which is technically not possible since the maximum tensile stress is obtained exactly for $l = l_0$ and cannot increase above l_0 . Hence the only solution is that no fracture arrest occurs for $\rho > \rho^{END}$. In fact, for a density of 300 kg/m^3 no fracture arrest was observed using the DE model (Fig. 13). For this simulation, we also tried with longer column lengths L up to 10 m which did not affect the full propagation. The corresponding maximum propagation distance for this case is about 2.3 m (for $l_{dyn}^* = l_0$), in agreement with field data for which the maximum propagation distance recorded was $l^* = 2.15 \text{ m}$ (Fig. 13b).

Obviously, the density ρ^{END} which was 280 kg/m^3 in our simulations, will vary depending on the geometry and material properties of the snowpack. For the cases presented in Figs. 15b and 15c, the Young's modulus was derived from density [Eq. (3)], the slab thickness D was constant equal to 20 cm, the slope angle $\psi = 0^\circ$ (case #1). This set of parameters resulted in a density $\rho^{END} = 280 \text{ kg/m}^3$. However, for a slope angle of 23° and taking into account the dependence of slab thickness with slab density (Tab. 4), ρ^{END} would be even less than 200 kg/m^3 , as shown in Fig. 13b (case #2) since the transition between a regime of fracture arrest and full propagation is between 150 and 200 kg/m^3 . Furthermore, as the propagation distance is also strongly influenced by the WL thickness D_{wl} (Fig. 11b), we assume that ρ^{END}

increases with D_{wl} as the maximum tensile stress in the slab increases with D_{wl} .

4 Discussion

In this study, a numerical model based on the discrete element method was developed in order to perform numerical PST simulations and study the mechanical processes involved. Despite the apparent simplicity of the proposed DE model and of the structure of the simulated WL, we were able to quantitatively address the issue of the dynamic phase of crack propagation as well as fracture arrest propensity and to reproduce PST field data.

First, a parametric analysis was conducted to study the influence of snowpack properties on crack propagation speed and distance. It was shown that the propagation speed increases with increasing slab density ρ , slab Young's modulus E , slab thickness D and slope angle ψ . The propagation speed was almost not influenced by WL thickness. The increase of crack propagation speed with slab density is not compatible with the expression for crack propagation speed proposed by Heierli (2008) for which the speed decreases with increasing slab density ρ (for a constant value of the Young's modulus of the slab), as for a crack in a homogeneous material (Auld, 1973). However, this is obviously not the case here, since the crack propagates through the underlying WL. Therefore, the propagation speed is likely to decrease with increasing WL density (and thus to increase with

increasing WL porosity) but to increase with slab density, as shown by our results.

In addition, it was shown that the tensile fracture of the slab always starts from the top surface of the slab. The propagation distance l^* increases with increasing tensile strength of the slab σ_t , slab thickness D and slope angle ψ . The latter result suggests that slab bending is the primary process influencing the tensile failure of the slab which corroborates the conclusions of van Herwijnen et al. (2010). In contrast, the propagation distance decreases with increasing slab Young's modulus E , slab density ρ and WL thickness D_{wl} . These results are in agreement with Gaume et al. (2015) who showed that the tensile failure probability (fracture arrest propensity) decreased with increasing tensile strength σ_t of the slab, increased with increasing Young's modulus E of the slab and decreased with increasing slab thickness D . This latter model is based on the finite element method and takes into account the weak layer strength heterogeneity, stress redistributions by elasticity of the slab, the possible tensile failure of the slab as well as dynamic effects. However, the weak layer was modeled in their approach as an interface and the bending of the slab induced by the collapse of the weak layer was not accounted for.

Furthermore, by accounting for the relation between the mechanical properties of the snowpack, the increase of crack propagation speed and distance with increasing slab density was well reproduced. The slight overestimation of the propagation speed for low densities might be due to the fact that, to compute the propagation speed, the slab was considered as purely elastic and possible plastic effects in the slab that might induce energy dissipation were disregarded. The in-depth analysis of the mechanical processes involved in fracture arrest showed that after a certain slab density value ρ' , the evolution of the maximum tensile stress in the slab with slab density diverged from the static beam theory. This is due to dynamic effects during crack propagation that induce a loss of support of the slab where the stresses do not have time to establish. Ultimately, for a density ρ^{END} , the maximum tensile stress in the slab decreases below its tensile strength leading to full propagation without fracture arrest. Consequently, for large densities, mechanical properties of the snowpack only marginally affect crack propagation distance. In that case, terrain characteristics and snowpack spatial variability will play a crucial role in the definition of the release area.

In addition, interestingly, in very few simulations both fracture arrest by tensile failure of the slab and full propagation was observed. In these cases, a portion of the WL on the right-side of the slab tensile crack was damaged over a sufficient length to exceed the critical length leading again to crack propagation. This process repeated itself until the end of the system leading to so-called "en-echelon" fractures (Van Herwijnen, 2005; van Herwijnen et al., 2010; Gauthier and Jamieson, 2010). This is likely to happen for very unstable conditions (very low critical length) but for a slab of

intermediate density, not too dense so fracture arrest can occur and not too loose so that the crack can still propagate.

Concerning the limitations of the model, we recall that the triangular shape of the WL structure is highly idealized and that more complex and more realistic geometries might have an influence on the presented results. In the future, the micro-structure of the WL could be derived from micro-tomographic images (Hagenmuller et al., 2014) in order to perform more realistic simulations. In addition, whereas we applied our model for cases for which the bending of the slab is important, our approach could still be used for cases with thinner weak layers and thus much lower amplitude of bending. Moreover, we would like to recall that the crack propagation speed was computed from the vertical displacement wave of the slab. However, for high values of the slope angle ψ , the collapse only constitutes a secondary process and the tangential displacement during propagation becomes higher than the vertical displacement. Typically, for $\psi > 40^\circ$, it is not possible to compute the propagation speed using the presented approach as the height of collapse becomes too low. An analysis of the tangential displacement revealed that the crack propagation speed on slopes where the shear component of the slab weight is very important ($\psi > 40^\circ$) might be significantly higher than the propagation speed on gentle slopes. This analysis suggested propagation speeds up to 150 m/s, similar to those reported for real-scale avalanches by Hamre et al. (2014). However, they considered avalanches triggered artificially by explosives leading to even more complex interactions due to the propagation wave of the blast.

With regards to practical applications, the results of our study can help to choose the size of the column length in field PSTs. Indeed, we showed that the maximum length for which snowpack properties might affect the propagation distance is around 2 m, in agreement with the study of Bair et al. (2014). However, this result does not mean that all PSTs should be 2 m long. The chosen column length can be evaluated from slab thickness and density. As shown by Figs. 11 and 13, slab Young's modulus and tensile strength which are related to slab density, as well as slab thickness strongly affect the propagation distance. Hence, for soft and relatively thin slabs, the standard column length of 1.2 m might be sufficient. However, for very strong and thick slabs, the column length should not be lower than 2 m in order to be able to still observe a possible arrest of the fracture due to slab tensile failure. If slab fracture is not observed in a PST for a column length of 2 m, fracture arrest is likely to be mainly driven by terrain and snowpack spatial variability and a 3D-terrain model including the snowpack might be required to evaluate where fracture arrest might occur (Veitinger et al., 2014).

5 Conclusions

We proposed a new approach to characterize the dynamic phase of crack propagation in weak snowpack layers as well as fracture arrest propensity by means of numerical PST simulations based on the discrete element method with elastic-brittle bonded grains.

This model allowed us to compute crack propagation speed from slab vertical displacement as a function of snowpack properties. Furthermore, crack propagation distance was computed by taking into account the tensile strength of the slab. A parametric analysis provided the crack propagation speed and distance as a function of the different snowpack properties. We showed that the propagation speed increases with increasing Young's modulus of the slab, slab depth, slab density and slope angle but decreases with increasing weak layer strength. The propagation distance decreases with increasing Young's modulus of the slab, slab density and weak layer thickness but increases with increasing slab tensile strength, slab depth, weak layer strength and slope angle.

Then, the existing relationship between slab thickness, Young's modulus and tensile strength with density was implemented. Accounting for this relationship, modeled propagation speed and distances were found in good agreement with those obtained from field measurements with the propagation saw test. In particular, for densities ranging from 100 to 300 kg/m³, the propagation speed increased from approx. 10 to 50 m/s and the propagation distance was found to increase from approx. 0.4 m to 2 m (column length). Concerning the mechanical processes, the static beam theory predicts an increase of the maximum tensile stress with increasing density. However, we show that dynamic effects of crack propagation induce a loss of support of the slab which increases with increasing crack propagation speed and thus slab density. This produces a decrease of the maximum stress with density which ultimately becomes lower than the tensile strength of the slab for a critical density ρ^{END} leading to the absence of slab tensile fracture and thus wide-spread crack propagation. According to our simulations, this critical density depends mostly on slab and WL thicknesses and slope angle. It decreases with slab depth and slope angle but increases with WL thickness.

For slab layers denser than ρ^{END} , the slab tensile fracture in the field and thus the potential release area will mostly be controlled by topographical and morphological features of the path such as ridges, rocks, trees, terrain breaks, etc. but also by the spatial heterogeneity of the snow cover. In addition, we showed that the maximum propagation distance associated with the density ρ^{END} was around 2 m, justifying why the column length of a propagation saw test should not be lower than 2 m for hard snow slabs, in order to be able to observe fracture arrest. This result is in agreement with the recent study of Bair et al. (2014) about PST edge effects.

In the future, an in-depth analysis of crack propagation speeds for large slope angles will be carried out in order to distinguish the speed associated with the collapse wave of the slab and the speed associated to its tangential displacement. Finally, different and more complex structures for the WL will also be implemented with the long-term objective to model the structure of the WL directly from segmented micro-tomographic images (Hagenmuller et al., 2013).

Appendix A: Evaluation of the crack propagation speed

The method to derive the crack propagation speed from the evolution of the vertical displacement of the slab in field and simulated PSTs is the same as that described in van Herwijnen and Jamieson (2005). This appendix provides details about this procedure and its application for two simulation and one experiment examples. The first example is a simulation for a density $\rho = 250$ kg/m³ and a Young's modulus $E = 4$ MPa (Fig. A1a) and the second example is a simulation for the same density but with a Young's modulus derived from density according to Scapozza (2004), $E = 7.8$ MPa (Fig. A1b) corresponding to the displacement evolution shown in Figure 6. The third case (Fig. A1c) corresponds to an experiment with a density $\rho = 240$ kg/m³. In detail, for each simulation or experiment, a vertical displacement threshold s is defined that allows to evaluate the position x of the crack tip as a function of time (see insets of Fig. A1). A linear fit to these curves allows to evaluate the propagation speed as a function of the vertical displacement threshold s (Fig. A1). Then, the crack propagation speed is taken as the average propagation speed (over the displacement threshold s) during the dynamic propagation phase where the propagation speed appears to be stable with the displacement threshold (average between s_1 and s_3). Note that different methods could have been used to compute the propagation speed but we wanted to have exactly the same procedure for both the experiments and the numerical simulations for the sake of the comparison.

Acknowledgements. We thank Pascal Hagenmuller, an anonymous reviewer and the associate editor Eric Larour for their valuable comments and remarks that helped us to improve our paper. J. Gaume was supported by a Swiss Government Excellence Scholarship and is grateful to the State Secretariat for Education, Research and Innovation SERI of the Swiss Government. Benjamin Reuter, Eric Knoff and Mark Staples assisted with field data collection.

References

- Auld, B. A.: Acoustic fields and waves in solids, Ripol Classic, 1973.
- Bair, E., Simenhois, R., van Herwijnen, A., and Birkeland, K.: The influence of edge effects on crack propagation in snow stability tests, *The Cryosphere*, 8, 1407–1418, 2014.

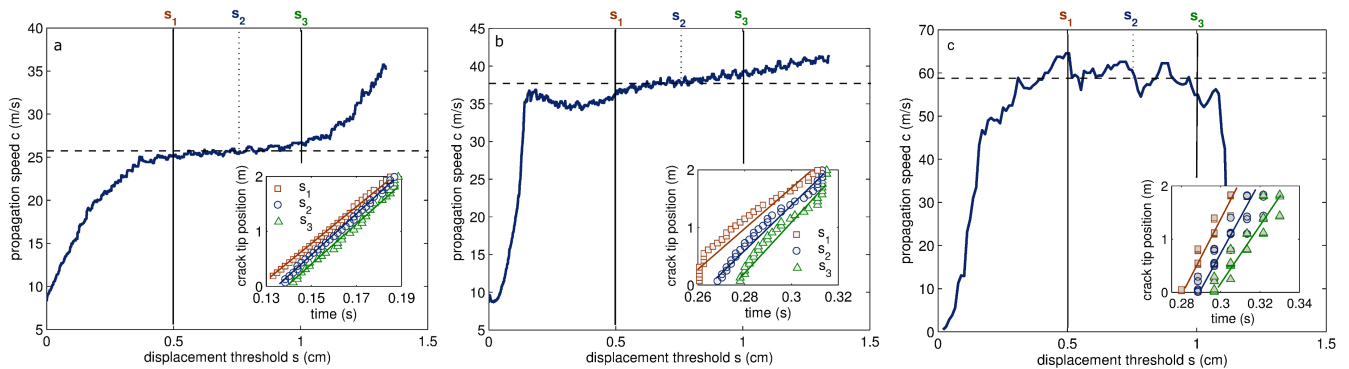


Figure A1: Propagation speed as a function of the vertical displacement threshold s . The insets represent the crack tip position as a function of time for 3 vertical displacement thresholds. The lines correspond to a linear fit. (a) simulation for $\rho = 250 \text{ kg/m}^3$, $E = 4 \text{ MPa}$, $D = 20 \text{ cm}$, $\psi = 0^\circ$; (b) simulation for $\rho = 250 \text{ kg/m}^3$, $E = 7.8 \text{ MPa}$, $D = 20 \text{ cm}$, $\psi = 0^\circ$ (c) experiment for a density $\rho = 240 \text{ kg/m}^3$.

Bair, E. H., Simenhois, R., Birkeland, K., and Dozier, J.: A field study on failure of storm snow slab avalanches, *Cold Regions Science and Technology*, 79, 20–28, 2012.

Birkeland, K., van Herwijnen, A., Knoff, E., Staples, M., Bair, E., and Simenhois, R.: The role of slab and weak layers in fracture arrest, in: P. Haegeli (Editor), 2014 International Snow Science Workshop, Banff, Alberta, pp. 156–163, 2014.

Camborde, F., Mariotti, C., and Donzé, F.: Numerical study of rock and concrete behaviour by discrete element modelling, *Computers and geotechnics*, 27, 225–247, 2000.

Cambou, B. and Jean, M.: *Micromécanique des matériaux granulaires*, 2001.

Chandel, C., Mahajan, P., Srivastava, P., and Kumar, V.: The behaviour of snow under the effect of combined compressive and shear loading, *Current Science*, 107, 888, 2014.

Chaudhuri, B., Mehrotra, A., Muzzio, F. J., and Tomassone, M. S.: Cohesive effects in powder mixing in a tumbling blender, *Powder Technology*, 165, 105–114, 2006.

Chiaia, B., Cornetti, P., and Frigo, B.: Triggering of dry snow slab avalanches: stress versus fracture mechanical approach, *Cold Reg. Sci. Technol.*, 53, 170–178, 2008.

Crocker, J. C. and Grier, D. G.: Methods of digital video microscopy for colloidal studies, *Journal of colloid and interface science*, 179, 298–310, 1996.

Cundall, P. A.: Numerical experiments on localization in frictional materials, *Ingenieur-archiv*, 59, 148–159, 1989.

Cundall, P. A. and Strack, O. D. L.: A discrete numerical model for granular assemblies, *Géotechnique*, 29, 47–65, 1979.

da Cruz, F., Emam, S., Prochnow, M., Roux, J.-N., and Chevoir, F.: Rheophysics of dense granular materials: Discrete simulation of plane shear flows, *Physical Review E*, 72, 021 309, 2005.

Faug, T., Beguin, R., and Chanut, B.: Mean steady granular force on a wall overflowed by free-surface gravity-driven dense flows, *Physical Review E*, 80, 021305, 2009.

Gaume, J., Chambon, G., and Naaim, M.: Quasistatic to inertial transition in granular materials and the role of fluctuations, *Physical Review E*, 84, 051 304, 2011.

Gaume, J., Chambon, G., Eckert, N., and Naaim, M.: Influence of weak-layer heterogeneity on snow slab avalanche release: Appli-

cation to the evaluation of avalanche release depths., *J. Glaciol.*, 59(215), 423–437, 2013.

Gaume, J., Chambon, G., Reiweger, I., van Herwijnen, A., and Schweizer, J.: On the failure criterion of weak-snow layers using the discrete element method, P. Haegeli (Editor), 2014 International Snow Science Workshop, Banff, Alberta, 2014a.

Gaume, J., Schweizer, J., van Herwijnen, A., Chambon, G., Reuter, B., Eckert, N., and Naaim, M.: Evaluation of slope stability with respect to snowpack spatial variability, *J. Geophys. Res.*, 119, 1783–1789, doi:10.1002/2014JF003193, 2014b.

Gaume, J., Chambon, G., Eckert, N., Naaim, M., and Schweizer, J.: Influence of weak layer heterogeneity and slab properties on slab tensile failure propensity and avalanche release area, *The Cryosphere*, 9, 795–804, doi:10.5194/tc-9-795-2015, http://www.the-cryosphere.net/9/795/2015/, 2015.

Gauthier, D. and Jamieson, B.: Towards a field test for fracture propagation propensity in weak snowpack layers, *J. Glaciol.*, 52, 164–168, 2006.

Gauthier, D. and Jamieson, B.: Evaluation of a prototype field test for fracture and failure propagation propensity in weak snowpack layers, *Cold Reg. Sci. Technol.*, 51, 87–97, 2008.

Gauthier, D. and Jamieson, B.: On the sustainability and arrest of weak layer fracture in whumpfs and avalanches, in: Proceedings of the International Snow Science Workshop, pp. 224–231, 2010.

Greene, E., Birkeland, K., Elder, K., Johnson, G., Landry, C., McCammon, I., Moore, M., Sharaf, D., Sterbenz, C., Tremper, B., et al.: Snow, weather, and avalanches: Observational guidelines for avalanche programs in the United States, American Avalanche Association, Pagosa Springs, Colorado, 150, 2004.

Hagenmuller, P., Chambon, G., Lesaffre, B., Flin, F., and Naaim, M.: Energy-based binary segmentation of snow microtomographic images, *Journal of Glaciology*, 59, 859–873, doi:10.3189/2013JoG13J035, 2013.

Hagenmuller, P., Theile, T., and Schneebeli, M.: Numerical simulation of microstructural damage and tensile strength of snow, *Geophys. Res. Lett.*, 41, 86–89, doi:10.1002/2013GL058078, 2014.

- Hagemuller, P., Chambon, G., and Naaim, M.: Microstructure-based modeling of snow mechanics: a discrete element approach, *The Cryosphere Discussions*, 9, 2015.
- 1100 Hamre, D., Simenhois, R., and Birkeland, K.: Fracture speed of triggered avalanches, in: P. Haegeli (Editor), *Proceedings ISSW*¹¹⁶⁰ 2014. International Snow Science Workshop, Banff, Alberta, Canada, 29 September - 3 October 2014, pp. 174–178, 2014.
- Heierli, J.: Anticrack model for slab avalanche release, Ph.D. thesis, Karlsruhe, Univ., Diss., 2008.
- 1105 Heierli, J., Gumbsch, P., and Zaiser, M.: Anticrack nucleation as¹¹⁶⁵ triggering mechanism for snow slab avalanches, *Science*, 321, 240, 2008.
- Hentz, S., Donzé, F. V., and Daudeville, L.: Discrete element modelling of concrete submitted to dynamic loading at high strain rates, *Computers & structures*, 82, 2509–2524, 2004. ¹¹⁷⁰
- Iwashita, K. and Oda, M.: Micro-deformation mechanism of shear banding process based on modified distinct element method, *Powder Technology*, 109, 192–205, 2000.
- 1115 Jamieson, B. and Schweizer, J.: Texture and strength changes of buried surface-hoar layers with implications for dry snow-slab¹¹⁷⁵ avalanche release, *J. Glaciol.*, 46, 151–160, 2000.
- Kusano, N., Aoyagi, T., Aizawa, J., Ueno, H., Morikawa, H., and Kobayashi, N.: Impulsive local damage analyses of concrete structure by the distinct element method, *Nuclear engineering and design*, 138, 105–110, 1992. ¹¹⁸⁰
- McClung, D.: Shear fracture precipitated by strain softening as a mechanism of dry slab avalanche release, *J. Geophys. Res.*, 84(B7), 3519–3526, 1979.
- 1125 Meguro, K. and Hakuno, M.: Fracture analyses of concrete structures by the modified distinct element method, *Structural engi-¹¹⁸⁵neering/earthquake engineering*, 6, 283–294, 1989.
- Podolskiy, E., Chambon, G., Naaim, M., and Gaume, J.: A review of finite element modelling in snow mechanics, *Journal of Glaciology*, 59, 1189–1201, 2013.
- 1130 Podolskiy, E., Barbero, M., Barpi, F., Chambon, G., Borri-Brunetto,¹¹⁹⁰ M., Pallara, O., Frigo, B., Chiaia, B., and Naaim, M.: Healing of snow surface-to-surface contacts by isothermal sintering, *The Cryosphere Discussions*, 8, 2465–2490, 2014.
- 1135 Radjai, F., Dubois, F., et al.: *Discrete-element modeling of granular materials*, Wiley, 2011. ¹¹⁹⁵
- Reiweger, I., Gaume, J., and Schweizer, J.: A new mixed-mode failure criterion for weak snowpack layers, *Geophys. Res. Lett.*, 42, doi:10.1002/2014GL062780., 2015.
- 1140 Rognon, P., Roux, J.-N., Naaim, M., and Chevoir, F.: Dense flows of cohesive granular materials, *Journal of Fluid Mechanics*, 596, 21–47, doi:10.1017/S0022112007009329, 2008.
- Roux, J.-N. and Combe, G.: Quasistatic rheology and the origins of strain, *Comptes Rendus Physique*, 3, 131–140, 2002.
- 1145 Sarkar, A. and Wassgren, C.: Continuous blending of cohesive granular material, *Chemical Engineering Science*, 65, 5687–5698, 2010.
- Scapozza, C.: Entwicklung eines dichte- und temperaturabhängigen Stoffgesetzes zur Beschreibung des visko-elastischen Verhaltens von Schnee, Ph.D. thesis, ETH Zürich, 2004.
- 1150 Schweizer, J., Jamieson, B., and Schneebeli, M.: Snow avalanche formation, *Rev. Geophys.*, 41(4), 1016, 2003.
- Schweizer, J., Reuter, B., van Herwijnen, A., Jamieson, B., and Gauthier, D.: On how the tensile strength of the slab affects crack propagation propensity, in: P. Haegeli (Editor), *Proceedings ISSW 2014. International Snow Science Workshop, Banff, Alberta, Canada, 29 September - 3 October 2014*, pp. 164–168, 2014.
- Sigrist, C.: Measurements of fracture mechanical properties of snow and application to dry snow slab avalanche release, Ph.D. thesis, ETH Zürich, 2006.
- Sigrist, C. and Schweizer, J.: Critical energy release rates of weak snowpack layers determined in field experiments, *Geophys. Res. Lett.*, 34, 2007.
- Szabo, D. and Schneebeli, M.: Subsecond sintering of ice, *Applied Physics Letters*, 90, 151 916, 2007.
- Timoshenko, S. and Goodier, J.: *Theory of Elasticity*, vol. 37, 1970.
- Van Herwijnen, A.: Fractures in weak snowpack layers in relation to slab avalanche release, Ph.D. thesis, University of Calgary, 2005.
- van Herwijnen, A. and Birkeland, K.: Measurements of snow slab displacement in Extended Column Tests and comparison with Propagation Saw Tests, *Cold Regions Science and Technology*, 97, 97–103, 2014.
- van Herwijnen, A. and Heierli, J.: Measurements of crack-face friction in collapsed weak snow layers, *Geophys. Res. Lett.*, 36, L23502, 2009.
- van Herwijnen, A. and Jamieson, B.: High speed photography of fractures in weak snowpack layers, *Cold Reg. Sci. Technol.*, 43(1-2), 71–82, 2005.
- van Herwijnen, A. and Jamieson, B.: Snowpack properties associated with fracture initiation and propagation resulting in skier-triggered dry snow slab avalanches, *Cold Reg. Sci. Technol.*, 50, 13–22, 2007.
- van Herwijnen, A., Schweizer, J., and Heierli, J.: Measurement of the deformation field associated with fracture propagation in weak snowpack layers, *J. Geophys. Res.*, 115, 2010.
- Veitinger, J., Sovilla, B., and Purves, R.: Influence of snow depth distribution on surface roughness in alpine terrain: a multi-scale approach, *The Cryosphere*, 8, 547–569, 2014.
- Zeidler, A. and Jamieson, B.: Refinements of empirical models to forecast the shear strength of persistent weak snow layers: PART B: Layers of surface hoar crystals, *Cold Reg. Sci. Technol.*, 44, 184–193, 2006a.
- Zeidler, A. and Jamieson, B.: Refinements of empirical models to forecast the shear strength of persistent weak snow layers PART A: Layers of faceted crystals, *Cold Reg. Sci. Technol.*, 44, 194–205, 2006b.



Reply to Referee #1

We thank Pascal Hagenmuller for his very interesting and constructive comments that helped us to significantly improve the quality of our paper.

We revised our paper in order to account for his remarks and we provide below detailed answers to the various issues raised by the reviewer.

Comment M1). *The abstract is written as an introduction and contains almost the same information as the introduction of the paper. Please consider significantly reducing the introduction part of the abstract (p610 11-15) and adding method description and the key results.*

Answer to comment M1). The abstract will be rewritten. In particular, the sentences between “For instance ... affect dynamic crack propagation” will be removed from the abstract leading to a reduction of 20%.

Comment M2). *The way the propagation speed is computed from field and numerical PST should be explicitly presented. This is described in the quoted reference (van Herwijnen and Jamieson, 2005). However, Figure 6 shows the temporal evolution of the computed vertical displacements and does not clearly reveal a “time delay between the onset of movement between markers proportional to the distance between the markers” (p613, l2-3). Consider adding some clarifications. If the definition of c is somehow ambiguous, it would be appropriate to focus only on l^* , which is, in my opinion, much more important in the context of avalanche forecasting and already discussed deeper in the paper.*

Answer to comment M2). As stated by the reviewer, the method to derive the propagation speed from field PSTs is explicitly and clearly described in van Herwijnen and Jamieson (2005). We used exactly the same procedure to derive the propagation speed from our numerical simulations. However, we agree that the application of this procedure to our simulations would benefit from further clarifications. Hence, we will provide an appendix showing the detailed procedure for the evaluation of the crack propagation speed and its application for two simulation examples. The first example is a simulation for a density $\rho = 250 \text{ kg/m}^3$ and a Young’s modulus $E = 4 \text{ MPa}$ (Fig. 1a) and the second example is a simulation for the same density but with a Young’s modulus derived from density according to Scapozza (2004), $E = 7.8 \text{ MPa}$ (Fig. 1b) corresponding to Figure 6 of the paper. The third case (Fig. 1c) corresponds to an experiment for a density $\rho = 240 \text{ kg/m}^3$. In detail, for each simulation or experiment, a vertical displacement threshold s is defined that allows to evaluate the position x of the crack tip as a function of time (see insets of Fig. 1).

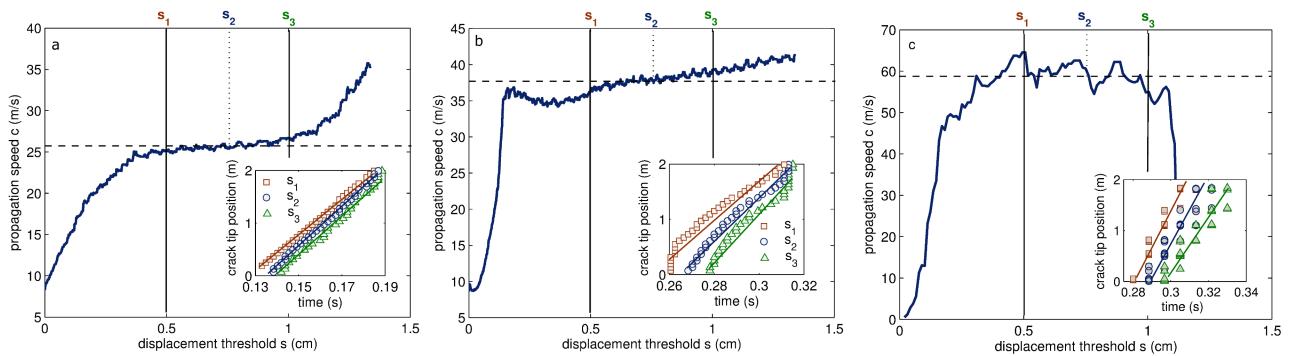


Figure 1: Propagation speed as a function of the vertical displacement threshold s . The insets represent the crack position as a function of time for 3 vertical displacement thresholds. The lines correspond to a linear fit. (a) simulation for $\rho = 250 \text{ kg/m}^3$, $E = 4 \text{ MPa}$; (b) simulation for $\rho = 250 \text{ kg/m}^3$, $E = 7.8 \text{ MPa}$, (c) experiment for a density $\rho = 240 \text{ kg/m}^3$.

A linear fit to these curves allows to evaluate the propagation speed as a function of the vertical displacement threshold s (Fig. 1). In some cases (e.g. inset of Fig. 1a), the increase of the crack position with time is perfectly linear. However, in a few cases (e.g. inset of Fig. 1b), this linearity is not perfect, especially at the moment of the onset and at the end of the propagation. Hence, the “time delay between the onset of movement between markers is proportional to the distance between the markers” only during the dynamic phase of crack

propagation but not during the transient phases of the onset and the end of propagation. Then, the crack propagation speed is taken as the average propagation speed (over the displacement threshold s) during the dynamic propagation phase where the propagation speed appears to be stable with the displacement threshold (average between s_1 and s_3). Note that different methods could have been used to compute the propagation speed but we wanted to have exactly the same procedure for both the experiments and the numerical simulations for the sake of the comparison.

Concerning the second comment of the reviewer about the relevance of the propagation speed to avalanche forecasting and his suggestion to focus on the propagation distance, we believe it is very important to also present and discuss the results about the propagation speed for two reasons:

- the propagation speed of a crack is deeply discussed in the avalanche community (Truman, 1973; Bohren and Beschta, 1974; Johnson et al., 2004; McClung, 2005, 2007; van Herwijnen et al., 2010; Hamre et al., 2014) but also more generally in the fracture mechanics community (e.g. Kanninen, 1968; Belytschko et al., 2003; Hsieh and Wang, 2004; Song et al., 2006; Lengliné et al., 2011). Our approach is the first one to compute the propagation speed of a crack in a multi-layered system from discrete element simulations and is thus highly scientifically relevant;
- the propagation distance was shown to depend strongly on dynamic effects and thus on the propagation speed of the crack. It is thus important to study the propagation speed to better understand fracture arrest propensity.

Comment M3). *p616, 14-9. The link between microscopic contact law parameters and macroscopic mechanical parameters is missing. The DE model is, for instance, described in terms of k_n , k_n^b and the results are described in terms of E . Note that this correspondence can be derived analytically without bi-axial tests. The reference to one non-reviewed proceeding is not sufficient.*

Answer to comment M3). The link between the contact properties (contact and bond stiffnesses k_n and \bar{k}_n) and macroscopic mechanical quantities (Young's modulus E) will be presented as well as more details about the contact model which is used also according to the reviewer's minor comment (11). In detail, the model which is used is a parallel bond model. It is represented schematically on Fig. 2 which will be added to the paper.

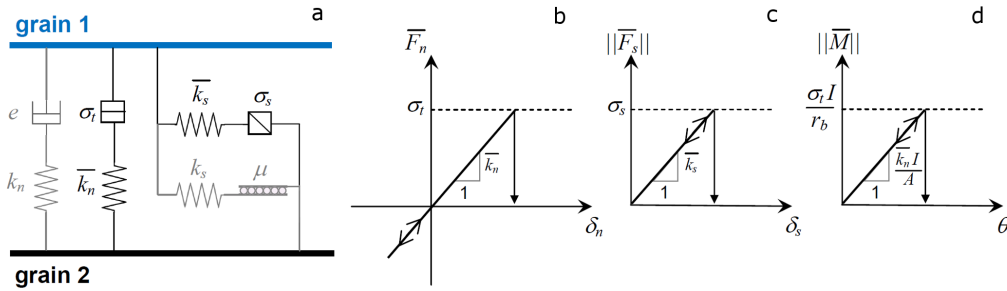


Figure 2: (a) Schematic representation of the parallel contact bond model which is used. The bonded part is represented in black while the unbonded part is represented in grey. (b) Bond normal force \bar{F}_n as a function of normal interpenetration δ_n between two grains. (c) Bond shear force $||\bar{F}_s||$ as a function of tangential interpenetration δ_s between two grains. (d) Bond bending moment $||\bar{M}||$ as a function of bending rotation θ between two grains.

Hence, the total stiffness of the bonded contact is equal to the sum of the contact stiffness k_n and the bond stiffness \bar{k}_n :

$$k_{tot} = k_n + \bar{k}_n$$

where $\bar{k}_n = k_n^b A$ where k_n^b is the bond normal stiffness per unit area and A the bond area. The dimension of k_n and \bar{k}_n is N/m while the dimension of k_n^b is Pa/m. As mentioned by the reviewer in the minor comments (11), the presentation of the model in terms of k_n (contact stiffness) and k_n^b (bond stiffness per unit area) might disrupt the reader. Since the contact area A was kept constant in the simulations, we decided to present the results in terms of k_n and \bar{k}_n which have the same dimensions.

Finally, in our case of a square grain assembly, the Young's modulus can be derived analytically from k_n and $\overline{k_n}$ according to:

$$E = \frac{1}{\pi R} (k_n + \overline{k_n}).$$

The contact stiffness k_n was kept constant at 1×10^4 N/m and $\overline{k_n}$ was varied between 1×10^3 and 1.5×10^6 N/m (for the slab) leading to realistic values of the Young's modulus E between 0.35 and 50 MPa. It was verified from biaxial tests that the macroscopic (bulk) Young's modulus of the slab effectively follows this relationship due to the specific (squared) structure of the slab.

All these new elements were added to the paper in section 2.2.2 Formulation of the model.

Comment M4). *section 3.2. The parametric study is done by changing a single variable. The complete parametric study by the authors is very interesting. As described by the authors, some parameters have the same effects on the computed PST. If possible, a parametric study with a few dimensionless numbers derived from a dimensional analysis would be welcome. With this method, the competition between the different mechanisms would appear clearly. If not possible, consider formulating explicitly the key results of this parametric analysis in conclusion, which is now missing. Explain why the parametric study does not consider the influence of the weak layer strength. Indeed, the authors suggest that the propagation speed is "mostly influenced by the load due to the slab and WL strength" (p618, l24-25).*

Answer to comment M4). We already tried to perform a dimensionless analysis with the results of the available simulations but it seems that the processes involved are very complex since no "simple" characteristic number could be highlighted. This will be however the focus of the future years' investigations in our group by performing more numerical simulations.

As suggested by the reviewer, the key results of the parametric study will be added to the conclusion of our paper.

Finally, concerning WL strength, we decided to focus in a first step on the influence of slab properties and WL thickness (which influences the amplitude of bending of the slab) on crack propagation speed and distance (this is already a lot of parameters to vary). However, as suggested by the reviewer and also to be consistent with the following statement in our manuscript "(...) mostly influenced by the load due to the slab and WL strength" we extended the parametric analysis to the WL strength (influence on propagation speed and on propagation distance) by adding two new graphs in Figs. 8 and 9 of the paper, as well as a paragraph of description in the text. However, the "strength" of the weak layer is vague since the weak layer has a complete failure envelope (see answer to comment M2 of Reviewer 2 as well as the new Figure 6 in the reply) with tensile, shear and compressive strengths (which are linked). We decided to present our results in terms of compressive strength σ_c^{WL} . The two new figures are provided below (Figures 3 and 4).

Comment M5). *Dynamic effects are shown to induce a transient loss of support of the slab. These dynamic effects might be sensible to the chosen time step and discretization scale (sphere radius). It is important to provide the order of magnitude of the speed of elastic waves (dependent on r) in the sample and to compare it to the crack propagation speed. The time step used in the DE simulation is also missing. Moreover, the parametric analysis do not include a sensitivity analysis to the sphere radius r . If r does not affect the simulation results, add this information briefly in the text (as it is done for the restitution coefficient, p615, l9-12).*

Answer to comment M5). Thanks for this suggestion. The time step Δt was computed as a function of grain properties according to

$$\Delta t = \sqrt{m/k} \approx r\sqrt{\rho/E}$$

where m and ρ are the smallest grain mass and density and k and E the largest contact/bond stiffness and Young's modulus, respectively. The choice of this time-step insures that the crack propagation speed is lower than the speed of the elastic waves in the sample. The order of magnitude of the speed of elastic waves in the sample is $c^e \approx \sqrt{E/\rho}$. For a low slab density $\rho = 100$ kg/m³ and a Young's modulus $E = 0.83$ MPa chosen according to Scapozza (2004), $c^e \approx 90$ m/s whereas the crack propagation speed is around 15 m/s. For a high density $\rho = 300$ kg/m³ and a Young's modulus $E = 16$ MPa chosen according to Scapozza (2004), $c^e \approx 230$ m/s whereas the crack propagation speed is around 45 m/s.

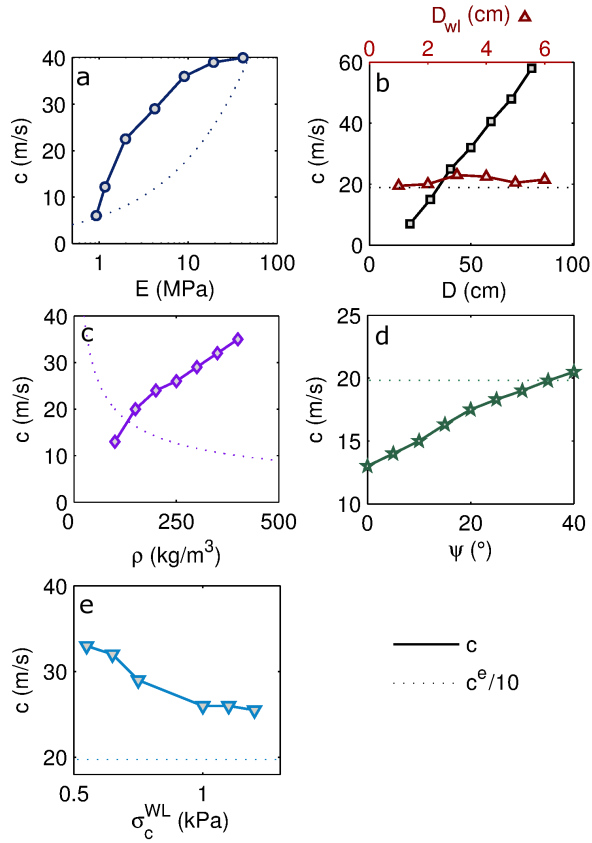


Figure 3: Crack propagation speed c (continuous lines) and speed of elastic waves in the slab $c^e/10$ (dotted lines) as a function of (a) the Young's modulus of the slab E , (b) slab and WL thicknesses D and D_{wl} , (c) slab density ρ , (d) slope angle ψ and (e) WL compressive strength σ_c^{WL} . The parameters used for these figures are given in Tab. 3.

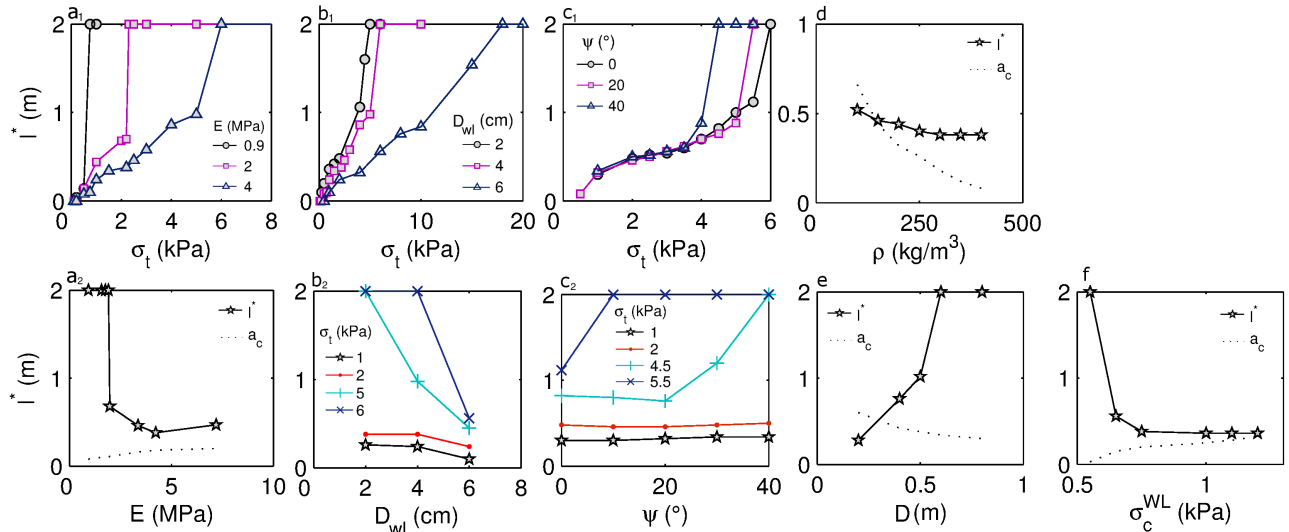


Figure 4: Crack propagation distance l^* as a function of the tensile strength σ_t and the Young's modulus E of the slab (a_1 - a_2), the tensile strength σ_t and the WL thickness D_{wl} (b_1 - b_2), the tensile strength σ_t and the slope angle ψ (c_1 - c_2), slab density ρ (d), slab thickness D (e) and WL compressive strength σ_c^{WL} (f). The parameters used for these plots are given in Tab. 3.

This information will be added to the manuscript in the “Formulation of the model” section (time-step), in the Results/Crack propagation speed section (the speed of the elastic waves will also be added inside Fig. 8 of our paper as you can see in Fig. 3 of the reply) as well as in the discussion (comparison of the crack propagation speed to the speed of the elastic waves in the sample).

The slab grains radius r has no influence on the results provided that it is small enough so that no size effects occur in order to obtain the correct Young’s modulus of the slab. However, changing the WL grain radius r_{wl} for a constant WL thickness would change its structure and would affect its strength. Hence, r_{wl} was kept constant. As suggested, this information was briefly added to the formulation of the model section.

Comment M6). *Comparison with field PST. The choices made to compare the numerical and experimental PST (Section 3.3, first paragraph) are unclear to me. I don't understand why two cases are distinguished. The size of the PST block, the slope angle, the slab density and weak layer thickness are variables which are certainly measured during the field experiments (“manual snow profile”, p612, 115-17). The only missing parameter is the weak layer strength. But this variable can be derived from the measured critical length, as done by the authors in case 2. So all input parameters of the DE model, E and σ_t being function of ρ , seem to be available. I don't understand the choices made in case 1 and case 2. The point of the authors is not clear and requires major clarifications.*

Answer to comment M6). The comparison between the numerical results and the experiments is a very important step of the paper. Hence we will significantly clarify the choices we made as it appeared unclear for the reviewer. Specifically, the reviewer is right when saying that we have access to all the mechanical and structural quantities from the PSTs except for the WL strength that can be derived from the critical length. However, the main issue is not the strength of the WL but its thickness which has been chosen constant for the comparison (nevertheless 6 different thicknesses were modeled for the parametric analysis). It is not possible at this stage and with the proposed discretization of the system (size of the slab grains) to model WLs of thickness lower than 1 cm, due to geometrical issues (placement of the triangles). It would be possible to model any WL thickness by reducing the size of the grains of the slab and substratum but would also be very time-consuming.

In addition, the results of the PSTs are prone to some variability (cf Figs. 10 and 11 of the paper) and we found it much more preferable to provide an overall trend of the propagation distance with density for two cases (constant depth or increase of depth with density) that could explain the general trend of the data. A similar choice was made by ? where the tensile failure probability was computed for two cases (constant depth or constant load) with similar trends in the results (see also comment 7).

Finally, it would be very time-consuming to simulate each field PST (121 PSTs).

Comment M7). *A few months ago, some of the authors have published an article in The Cryosphere Discussions entitled “Influence of weak layer heterogeneity and slab properties on slab failure propensity and avalanche release area” (December 2014). On contrary to the present paper, no dynamic effects and weak layer normal collapse are considered in the mechanical model (tell me if I am wrong). As noted (p628, 124-28), some of the numerical results in the two papers are in good agreement. I think it would be valuable if the authors could comment on this agreement, even the underlying implemented mechanisms are very different.*

Answer to comment M7). In our other paper now published in The Cryosphere (“Influence of weak layer heterogeneity and slab properties on slab failure propensity and avalanche release area”), the weak layer normal collapse was indeed not accounted for. However dynamic effects were also taken into account (see Gaume et al., 2013 for more details) in the finite element model. The good qualitative agreement between the results of these two different models (effect of E , ρ and D) was already discussed in the third paragraph of the discussion. Nevertheless, this part of the discussion will be expanded and detailed as suggested.

Minor comments

Comment m1). *p610, 115: all “ff” appears in a strange way on my printed version of the paper. Check with editing service whether it is normal.*

Answer to comment m1). It appears correctly in the online version our PC. Nevertheless, we will ask the editing service to check if it works correctly on every computers (linux, mac and PC).

Comment m2). p610, l19-24, "Then, the relation ... in PSTs". Awkward sentence. Reword. For instance, "In order to compare the numerical and experimental results, the slab mechanical properties (Young's modulus and strength) which are not measured in the field, were derived from slab density. The simulations are shown to fairly reproduce the field PSTs."

Answer to comment m2). Thanks. We will reword as suggested.

Comment m3). p611, l4, "if its size exceeds a critical length or if the load exceeds a critical value". The critical length already depends on the applied load, doesn't it?

Answer to comment m3). Yes but for a constant load, crack propagation requires the crack size to reach a critical length (which effectively depends on the load) and for a constant crack size (independent of the load), the load needs to exceed a critical value for the onset of crack propagation.

Comment m4). p611, introduction. A brief description of the PST would be welcome in introduction.

Answer to comment m4). This will be done.

Comment m5). p611, l19-21: "For instance, it is not uncommon to perform PST field measurements with widespread crack propagation on one day, while a few days later, with seemingly very little changes in snowpack properties, cracks will no longer propagate.". Quote appropriately.

Answer to comment m5). This sentence will be reworded: For instance, based on practitioners' experience, it is not uncommon to perform PST field measurements with widespread crack propagation on one day, while a few days later, with seemingly very little changes in snowpack properties, cracks will no longer propagate (Gauthier and Jamieson, 2008).

Comment m6). p613, subsection 2.2.1. This subsection should be incorporated to the global introduction

Answer to comment m6). We would like to keep this section here as it would increase significantly the size of the introduction and this paragraph justifies and motivates the use of our method (DEM) that we describe just in the next paragraph. We believe it would be too early to go into these arguments in the Introduction.

Comment m7). p614, l10: "completely rigid". Do you mean "fixed"?

Answer to comment m7). Yes, we mean that the substratum is fixed with completely rigid grains. This will be amended.

Comment m8). p614, l10: "simulations" – > "simulations (see Figure 4a)"

Answer to comment m8). This will be done.

Comment m9). p614, l12: "cubic" – > "square"

Answer to comment m9). Thanks. This will be changed.

Comment m10). p614, l15: "triangular form". It is impossible from the provided figures to see the exact form of the weak layer elements (nb spheres, angle). Moreover, it is unclear how the thickness of the weak layer is changed in the parametric study. I suggest deleting Figure 4b, which is useless in this form, and to replace it with a zoom on the weak layer structure.

Answer to comment m10). We will do exactly as suggested and provide a better figure (see new figure 5 below).

Comment m11). p615: I don't understand the role of the k_n and k_{bn} . If the bond is cohesive does the spring between grains play a role? Or is it a series of linear springs? Why is the value of k_n in N/m while k_n^b is in Pa/m?

Answer to comment m11). The parallel bond model we used will be precisely detailed as suggested by the review (see answer to comment M3 and the new figure of the contact model for more details).

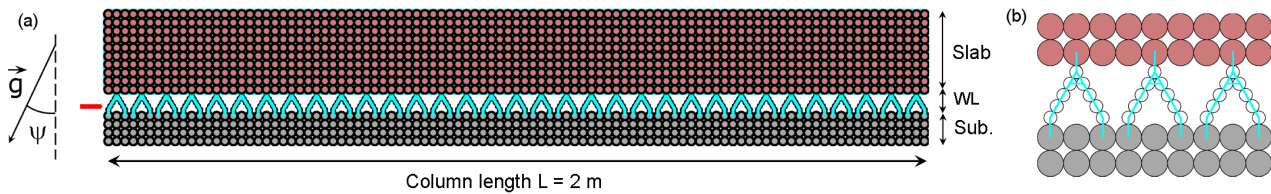


Figure 5: Simulated system of a Propagation Saw Test (PST) composed of a slab, a weak layer and a rigid substratum. The column is 2 m long. (b) Zoom on the weak layer structure. The blue lines represent the weak layer bonds.

Comment m12). p616,118-20: *"The only difference with the procedure for field measurements is that with DE we do not need markers since we have access to the displacement of every grain of the system."*. Delete.

Answer to comment m12). This will be done.

Comment m13). p618, 116 *"from almost zero"*. Give value.

Answer to comment m13). The sentence will be reworded. "from less than 5 m/s for very soft slabs ($E < 1$ MPa)".

Comment m14). p620,11: *"Hence, fracture arrest propensity decreases with slope angle."*. From Figures 9c1, 9c2, this conclusion does not appear as clear as stated. Be more precise on the cases where this conclusion applies.

Answer to comment m14). We will describe that the cases in which fracture arrest propensity decreases with slope angle correspond to high values of the tensile strength of the slab, typically higher than 4 kPa.

Comment m15). p620, 16-8: *"This interpretation is supported by the observation that the tensile opening of the crack always starts from the top surface of the slab in both DE simulations (Fig. 7) and in field PSTs."*. I do not agree. This observation only confirms that tension is due to slab weight projected along the slope AND bending. But it does not tell which mechanism is the more important.

Answer to comment m15). We agree and the sentence will be removed as well as in the Discussion p628 where this interpretation was recalled.

Comment m16). p621, 121-23: *I dont understand why different densities (240 and 250 kg/m3) are used? It is not very important for the comparison but it would make the presentation clearer. The comparison between Figure 3 and 6 would be also easier if the computed and measured displacements would be plotted on the same figure with the exact same marker position.*

Answer to comment m16). As already stated in the answer to comment M6, we do not want to reproduce exactly each PST, since the results are prone to some variability, but rather give some overall trends of the results. Here, this is the same, we do not pretend to be able to reproduce exactly the displacement of each individual experiment but rather show a good general agreement. We performed simulations for density steps of 50 kg/m^3 thus we compared a simulation of a density of 250 kg/m^3 to the closest density we had in the experiments (240 kg/m^3). The agreement is already remarkable. Showing figures 3 and 6 on the same graph, would be, according to us, misleading, since even if there is a good general agreement, there are some local differences between these two figures which would make the figures quite complex to understand.

Comment m17). p622, 119-22 *"The slight overestimation for low densities might be due to the fact that, to compute the propagation speed, the slab was considered as purely elastic and possible plastic effects in the slab that might induce energy dissipation were disregarded."*. I suggest to keep this idea for the discussion section.

Answer to comment m17). This will be moved to the discussion section.

Comment m18). p622, l25-28 *"This is not the case for the experiments for which the critical length generally increases with increasing density due to the associated increase of Young's modulus and a strengthening of the WL (Zeidler and Jamieson, 2006a, b; Szabo and Schneebeli, 2007; Podolskiy et al., 2014)". I don't understand what you mean.*

Answer to comment m18). We mean that during the season, for a given weak layer, the density of the overlying slab is increasing due to settlement. This induces not only a change in the Young's modulus (which was taken into account in the model), but also in general a strengthening of the weak layer (which was not accounted for). A higher strength leads to a higher critical length. This is in agreement with field measurements (citations above) which show an increase of the critical length with density. This sentence will be reworded and clarified.

Comment m19). p623, l3-6 *"Furthermore, for case 1,..., the better quantitative agreement with the experiments."* Awkward sentence. Reword.

Answer to comment m19). This will be reworded.

Comment m20). p623, l22-24 *"However, we argue that, as soon as fracture arrest occurs within the beam, the crack propagation distance is almost independent of the beam length."* I agree with your assumption. Since one of your conclusions (see abstract) is about column length, I suggest that you rapidly check your assumption with the model which is directly designed to do so.

Answer to comment m20). We already checked that for full propagation cases as stated p627 l10-12 (full propagation independent of the column length) but we also checked numerically the independence of the propagation distance to the beam length as well by doing simulations for longer beams to be sure that no size effects occur. This comment will be added to the paper.

Comment m21). p624, l5: σ_{xx} is not necessary tension. Moreover, indicate how the stress tensor is calculated from microscopic contact forces.

Answer to comment m21). We agree. Tensile stress will be replaced by normal stress throughout the text. The stress tensor was computed from contact forces using the classic Love homogenization formula (Cambou and Jean, 2001). This information will be added to the text.

Comment m22). p624, l18: "right side" – > "above the undamaged weak layer (right side in Figure 12).

Answer to comment m22). This will be changed as suggested.

Comment m23). p626, l3: "strength leading" – > "strength, leading"

Answer to comment m23). This will be changed.

Comment m24). p626, l9: "where stresses do not have time to establish". Do you mean that the displacement of the slab due to gravity is too slow to establish a mechanical equilibrium between bending and gravity?

Answer to comment m24). Yes this interpretation is more or less the same as what we wanted to highlight. This will also be added to the text as a clarification.

Comment m25). p626, l14-28: *In my opinion, the fit of the maximum tensile stress for density above 180 kg/m³ is not necessary and does not give additional information on the underlying mechanism. Delete and reword section appropriately.*

Answer to comment m25). We agree. The equation of the fit will be removed as well as the associated text.

Comment m26). Figure 2. Add scale in the figure on the right.

Answer to comment m26). The scale is already given by the width of the beam which is equal to 30 cm.

Comment m27). Figure 4. Replace subfigure 4b by a zoom on the WL structure

Answer to comment m27). Done. See our new figure 5 above.

Comment m28). *Figure 8. $m/s \rightarrow m s^{-1}$, $kg/m^3 \rightarrow kg m^3$*

Answer to comment m28). This will be done.

Comment m29). *Figure 9. Explain what is a_c in the caption of the figure*

Answer to comment m29). We will add in the caption that a_c represents the critical length for crack propagation.

Comment m30). *Figure 10. a) Explain to what correspond the boxplot (max, 75%, median, ... ??) b) Report the median value on the subfigure.*

Answer to comment m30). We will explain which quantities the boxplot represents. The median will also be added to Fig. 10b.

Comment m30). *Figure 12. Explain that σ_{xx} was linearly (?) interpolated between grains. The tensile stresses before failure appears to be very large (500 kPa 10 kPa) ???*

Answer to comment m30). Yes this is a simple linear interpolation between grains. This will be added to the caption. However, concerning the second remark, as explained to the second reviewer (comment M9), there is just a little mistake by us. The scale is of course not $\times 10^5$ but $\times 10^3$. We are sorry for this little mistake. The slab effectively breaks in tension for a stress $\sigma_{xx} = \sigma_t = 10$ kPa as predicted by Eq. 4. This will be corrected and thanks for pointing this out.

Reply to Referee #2

We thank Referee #2 for some valuable comments that helped us to improve our paper.

We revised our paper in order to account for some of the remarks but also provide arguments against some criticisms that were raised by the reviewer. In general, we argue that there is an important misunderstanding by the reviewer who believes that the properties that have been considered in this paper are the grain-grain contact properties and not the macroscopic (or “bulk” to use the term of the reviewer) ones. This is not the case. We clearly stated in the manuscript in section 2.2.3 that the contact properties have been calibrated to obtain the correct macroscopic (bulk) properties. If the reviewer might have been misled on this point, the substantial changes we made to the “Formulation of the model” section according to the comments of reviewer # 1 (better description of the contact law and of the link between contact and macroscopic properties) will clarify this point. In addition, a new paragraph will be written at the end of the “2.2.1 Motivation and objectives” section to make our point even clearer and precisely state the scale at which our model has to be considered. This new paragraph is provided in the Appendix of this reply.

We provide below detailed answers to the various issues raised by the reviewer.

Main comments

Comment M1). *The experimental design is questionable, however, and little attention is paid to the assumptions and motivations behind the particular numerical setup chosen.*

Answer to comment M1). The Propagation Saw Test (PST) is a very well-known and well-defined field test which is widely used in the avalanche community. The PST was concurrently developed by Gauthier and Jamieson (2006) and Sigrist and Schweizer (2007) and allows to determine crack propagation and fracture arrest propensity. As we wanted to evaluate the propagation speed and distance, the PST is very clearly the best existing set-up for our purpose as we can compare our numerical results to field data (the other possible set-up being the Extended Column Test which requires hand taping whose loading conditions are not well-controlled and whose results depend on the person conducting the test). In addition, note that, since the PST was invented, 8 years ago, more than 90 scientific publications (Google scholar) refer to this test. Actually, the main “questionable” parameter of the PST is the column length, which is discussed in this paper.

Comment M2). *Very little mention is made of the physical snow properties that govern actual avalanches or even the stability test (Propagation Saw Test or PST) that is being modeled. For example, it is well known that thick persistent weak layers are strongly anisotropic, with much weaker shear strength than compressive strength (Reiweger and Schweizer, 2010, 2013).*

Answer to comment M2). We do not agree. In fact, we describe the effect of snowpack properties (slab Young’s modulus E , slab tensile strength σ_t , slab thickness D , slab density ρ , slope angle ψ , WL thickness D_{WL}) on PST results (propagation speed and distance) and by extension on avalanche release through a very detailed parametric analysis (Sec. 3.2) and we even go further by taking into account the link between snowpack properties (Sec 3.3). Concerning, the anisotropy, our modeled weak layer has obviously a strong anisotropic shape leading also to a strongly anisotropic failure envelope. Furthermore, we clearly state in Sec. 2.2.3 that we carried out mixed mode shear compression loading tests in Gaume et al. (2014) of the WL to assess its failure envelope. Its failure envelope is strongly anisotropic with effectively much weak shear strength than compressive strength as shown in Gaume et al. (2014).

In order to make this point even clearer, we will add a new figure (see Fig. 6 below) to clearly show the anisotropic failure envelope of the modeled WL. In addition, we will refer to “anisotropic” in the context of the failure envelope in this section.

Comment M3). *It is also well known that there is very often a distinct difference in both hardness and grain size between the slab and the weak layer (e.g. Schweizer and Jamieson, 2007; DeVito et al., 2013), with the weak layer often having larger grains the opposite of what was modeled. These important physical foundations of the avalanche problem seem to have not been considered in the numerical study, though they could have and indeed should have for such a discrete modeling exercise.*

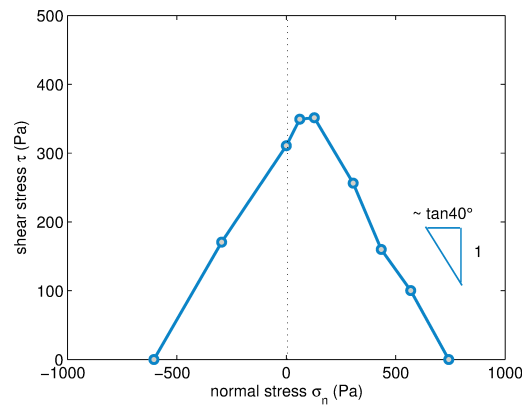


Figure 6: Failure envelope of the modelled WL obtained from mixed-mode shear-compression loading tests.

Answer to comment M3). The grain size of the slab has no importance on the simulation. It was chosen large enough for computational reasons and small enough to not cause size-effects. The only important parameters for the slab are the resulting macroscopic (or bulk as the reviewer says) Young’s modulus E and tensile strength σ_t . Similarly, for the weak layer, we could have achieved the same macroscopic (or bulk) failure envelope with different grain sizes by adapting the bond strength. Please, see also our new paragraph in Section 2.2.1 provided in the Appendix (see below).

Comment M4). *No mention is made of why the particular triangular stacking scheme for building the weak layer was chosen, nor for whether this gives the weak layer any anisotropy. Indeed, the word anisotropy does not appear even once in the manuscript, yet this is a fundamental characteristic of avalanche weak layers.*

Answer to comment M4). It is clearly stated in our manuscript that the “WL is composed of (..) a complex packing of collapsible triangular forms aimed at roughly representing the porous structure of persistent WLs such as surface hoar or depth hoar”. Such a structure has a strongly anisotropic failure envelope. However, as stated above, a new figure (Fig. 6) will be added to clearly show this anisotropy and a small paragraph will be also added to even better justify the choices made with regard to field and laboratory experiments on the failure of weak snow layers. Indeed, it was recently observed in field and laboratory experiments that the shear strength decreases with increasing compressive stress (Reiweger et al., 2015; Chandel et al., 2015). This very important feature can be reproduced with the used WL structure. The chosen WL structure allows to have different modes of failures (tension, shear, compression and mixed-mode) such as real weak snow layers and thus has the essential characteristics to model slab avalanche release. In addition, the word “anisotropy” will also be added to characterize the failure envelope which is weaker in shear than in compression.

Comment M5). *I am not convinced that any of the physical insights gleaned from the numerical sensitivity study are meaningful because little attention was given to the physical foundation of the model setup.*

Answer to comment M5). We do not agree. In contrary, most of the essential physical ingredients relevant to dry-snow slab avalanche release have been considered (elasticity of the slab, possible tensile failure of the slab, collapsible and anisotropic nature of the WL with a failure envelope allowing different failure modes). We do not see any other model that accounts for so many of the relevant ingredients as well as dynamic effects on the same time. This model is the first to reproduce not only qualitatively but also quantitatively the propagation speed and distance of field PST with such a good accuracy without any fitting of the model parameters (we recall that the contact properties have been calibrated in order to obtain the proper macroscopic/bulk properties, see also our new paragraph 2.2.1 provided in Appendix). We strongly contend that the underlying processes and physics of avalanche release are extremely well reproduced by our model as also shown by the good agreement between model and experimental results.

Comment M6). *Regarding the model formulation (Section 2.2.2.): the spherical grains used in the slab (1 cm) are about an order of magnitude larger than the typical snow grains in a natural snow slab. Although you can tune the density in the model to match the bulk density that you are interested in, this is only relevant for*

getting the overall gravitational loading correct. This completely ignores the number and strength of bonds and contacts in the discrete slab assembly, which is what is actually important from the perspective of slab stiffness, bulk strength, and the ability to propagate a stress wave.

Answer to comment M6). There seems to be, as stated in the very beginning of our reply, a misunderstanding by the reviewer on this part. In contrast to what the reviewer thought, we did not only get the overall gravitational loading correct, but also the stiffness (Young's modulus) and the macroscopic (bulk) tensile strength. Indeed, we performed numerically classic biaxial tests to derive the macroscopic (bulk) quantities from the grain-grain contact properties and validate the analytical relationship. The quantities that are presented throughout the paper (density ρ , Young's modulus E and tensile strength σ_t) are the macroscopic (bulk) quantities which were derived from the microscopic ones. This was already clearly stated in the manuscript in section 2.2.3 (Quote from our paper: "First, the macroscopic properties of the slab have to be determined as a function of the microscopic properties of the bond. Hence, bi-axial tests were carried out and allowed to determine the macroscopic Young's modulus of the slab as a function of the bond stiffness"). Besides, we recall that the size of the slab grains has no physical meaning, it is an entity of discretization. It was chosen large enough for computational reasons and small enough to avoid size effects. The slab should be seen, contrary to the weak layer, as a continuous material, discretized using the DEM and whose important parameters are the resulting macroscopic (bulk) Young's modulus and tensile strength. The method is commonly used to study the fracture of concrete under high loading rates (e.g. Hentz et al., 2004). Please, see also our new paragraph in Section 2.2.1 provided in the Appendix.

Comment M7). *Instead of focusing solely on getting the bulk density correct, and then assuming that the model is valid, there are a number of other ways that you could set up and validate such a model. As mentioned above, a numerical hardness test should give similar values as in a real slab. Since you're interested in slab fracture as a mechanism of fracture arrest, then you should also conduct some bulk strength tests to confirm that the tensile strength of the slab as a whole (not the individual bonds) corresponds with published strength values (e.g. the actual scale of beam experiments such as Sigrist et al. (2005) could be simulated to validate your model).*

Answer to comment M7). We actually performed classical bulk tests which are way more informative from a mechanical point of view than the ones (hardness and bulk strength tests) the reviewer suggests. We did biaxial tests which are the most classical (triaxial in 3D) tests to derive macroscopic (bulk) quantities such as Young's modulus and strength from contact properties. This well defined test (biaxial) is one of the basic tests in soil mechanics but not very well-known in the snow and avalanche community.

Comment M8). *Although widely used, the density is not an appropriate proxy for the strength and microstructure of snow, a fact that has been recognized for decades (Mellor, 1975; Shapiro et al., 1997). It's a shame not to recognize this given that this sort of discrete model setup holds such promise for moving beyond the limitations of density as the sole and predominant proxy measure in snow mechanics.*

Answer to comment M8). We recall once again that our model is not meant to reproduce the full microstructure of the slab (impossible at the scale of a PST), which is viewed here as a continuous material. We thus need to use proxys to evaluate the strength of this layer. For slab layers that are rather uniform, it has been shown that the density was an excellent proxy for Young's modulus and tensile strength as shown in McClung (1979); Jamieson and Johnston (1990); Scapozza (2004); Sigrist (2006). Furthermore, recently, Hagenmuller et al. (2015) showed, using microstructure-based discrete element modeling that the microstructure (snow type) had very little influence on the compressive behaviour of snow and that density was the best proxy.

Comment M9). *Figure 12 makes my point here. You are modeling a slab with a bulk density of 250 kg/m³, for which Eq. 4 suggests you should have a tensile strength of around 10 kPa. Of course, this equation came from bulk snow strength measurements from beam bending experiments, but you are using it for an ice grain contact law. In any case, the tensile fracture in your experiment, which originates at the top of the beam somewhere between the 5th and 6th panel in the figure, occurs when the tensile stress at the top of the beam is on the order of 100 kPa. So your bulk slab strength is an order of magnitude too high. You should be constructing the model such that your bulk model results agree with bulk snow measurements, which is not the approach you have taken here.*

Answer to comment M9). Actually, for this point, the reviewer was misled by a mistake we made in Fig. 12. This mistake was also noticed by the first reviewer. The scale is of course not $\times 10^5$ but $\times 10^3$. We are sorry for this mistake but this answers the reviewer's concern since the slab effectively breaks in tension for a stress $\sigma_{xx} = \sigma_t = 10$ kPa as predicted by Eq. 4. We recall here that the tensile strength values reported in our study are the macroscopic (bulk) values. The correction of this error in Fig. 12 plus the many amendments that will be made to our paper according also to comments by reviewer #1 will clarify this issue of the link between microscopic (contact) and macroscopic (bulk) properties.

Comment M10). *In the absence of any such rigorous validation exercise, the results of the present study amount to the use of a highly tunable model to reproduce a particular phenomenon, but not necessarily for the right physical reasons*

Answer to comment M10). As stated above, none of the model parameters were “tuned” to get a good agreement with field data. The proper bulk properties of the slab (Young's modulus E , tensile strength σ_t , density ρ) and of the WL (failure envelope) were obtained by calibrating the contact bond properties as classically done to model concrete fracture (e.g. Hentz et al., 2004).

Specific comments

Comment m1). *A distinction should be made between thick, collapsible weak layers of the type considered in this study and weak interfaces between adjacent layers, that may not be collapsible beyond grain scale effects that are relatively unimportant in the energy balance. The latter type is also responsible for slab avalanche activity, and this type of weakness is usually not amenable to performing the PST. The results of the present study, and any conclusions you attempt to draw about avalanches in general from this sort of exercise, are limited to the former case. This should be explicitly stated.*

Answer to comment m1). We do not see the point of distinguishing these different layers. A perfect interface does not exist in reality. The local breaking of bonds will always induce locally a volumetric response. It is not because you don't see it that it does not exist. The only reason why a PST could not be performed is that the thickness of the weak layer is lower than the thickness of the saw but this should not be a reason to distinguish between these layers. If we focused our paper on cases for which the bending of the slab is important, our approach could still be used in cases with much lower amplitudes of bending. This information will however be added to our paper in the discussion.

Comment m2). *Why the focus on crack speed and propagation distance in the paper? I don't understand the motivation for choosing these two metrics. What about the cut length? The cut length is the primary measurement in the field test, so why not more discussion of this in the model? Especially important would be any slope angle dependence on the cut length*

Answer to comment m2). We focused on the dynamic phase of crack propagation and our motivations are clearly stated in the abstract and introduction (the dynamic phase is not very well documented and understood). Of course our model also allows to obtain the conditions for the onset of crack propagation i.e. to obtain the critical length but this will be the subject of a further paper, focused only on the onset phase. We presented these results in the last European Geoscience Union (Gaume et al., 2015) and the paper is in preparation.

Comment m3). *It would actually be possible, and very interesting, to characterize the hardness of the discrete slab and weak layer assemblies by performing proxy numerical measures of cone (Johnson and Schneebeli, 1999; Schneebeli et al., 1999, e.g.) or blade penetration (Borstad and McClung, 2011) resistance. This seems obvious to me since you are essentially performing the same kind of experiment by indenting your weak layer with a numerical saw. Can you report the reaction force encountered by this saw in the model? This sort of metric would help to test and calibrate the method of choosing the discrete grain size and contact/cohesive law parameters.*

Answer to comment m3). As already stated in the main comments, we performed more powerful tests than cone penetration tests to characterize the hardness of our assemblies (biaxial tests). However, we agree, that, in the future, modelling for example a Snow Micro Pen (SMP) in a discrete assembly would surely help to better interpret SMP field results. This will be a part of our future modelling efforts. However, for this purpose, the microstructure of the snow will have to be reconstructed from microtomographic images such as in Hagemuller et al. (2015) since the physical processes at play leading to the SMP signal result from different and much smaller scales than those presented in this study.

Comment m4). *In the PST, slab fractures and the associated arrest are almost always within several slab thicknesses ahead of the saw, which is precisely the location of the maximum tensile stress at the surface of the slab (which can be shown via the same beam theories that you reference, but you see the same thing in Figure 7). This indicates that the fracture arrest is rather a structural arrest caused by the bending induced by the saw cut, that in turn fractures the slab. In other words, it is an artefact of the test itself, and may not be fundamental in actual avalanches (the en-echelon style of fracturing may be a specialized exception). This is also important because the collapse occurs after the propagation of the initial localized fracture (Reiweger et al., 2015; McClung and Borstad, 2012). For these reasons I think it is important to also report the propagation distance beyond the end of the saw, instead of (or in addition to) your new definition of propagation distance.*

Answer to comment m4). Actually, except in very few cases in which the slab fracture is directly caused by the bending induced by the saw cut (e.g. for very low slab densities in Fig. 9d and/or very low slab depth in Fig. 9e), the slab fracture occurs during the dynamic crack propagation which is uninfluenced by the saw (the onset of crack propagation could be induced by a skier for instance). In addition, even for an actual avalanche, similarly the important distance for bending induced stress and for the avalanche size will be the distance from the very first failure initiation point (whatever the nature of the initial trigger), to the location of the slab tensile failure and not from the crack tip at the moment of the onset of crack propagation. We will consider this interesting point by adding a new paragraph in the Discussion section. In addition, the distance between the onset or crack propagation and slab tensile failure can be easily derived from the propagation distance which is reported in our paper, since the critical length is also provided (Fig. 9). Adding this other distance to the graphs would thus be redundant and would affect their clarity.

Comment m5). *p 613, line 19: these do not appear to be snow dynamics references, yet are mentioned as such*

Answer to comment m5). The word “Snow” will be removed.

Comment m6). *p 614, line 5: were the tests actually performed, or will they be in the future? confusing use of tense here*

Answer to comment m6). Thanks, the Discrete Element propagation saw tests have of course been performed and the tense will be changed in this paragraph to clarify this.

Comment m7). *a better schematic diagram is needed for the contact and cohesive law used in the model*

Answer to comment m7). Done. See answer to reviewer # 1.

Comment m8). *p 615, line 12: does this mean viscous effects are minimal? The discussion of the restitution coefficient, and the lack of sensitivity, are a bit confusing. If indeed this has to do with the influence of viscous effects on the timescale of the simulated/actual PST, then this should probably be discussed further.*

Answer to comment m8). The coefficient of restitution and globally viscous terms have no effects in our case due to the presence of the cohesive part of the contact law. These effects are generally important for studies in which new contacts/collisions occur. In our case, the results are mostly driven by bond breaking which explains why the coefficient of restitution has no influence on the presented results. This will be clarified.

Comment m9). *Section 2.2.3, first paragraph: this is not a very clear description, and the reference to the protocol is not peer reviewed. Perhaps some of this addresses my concerns about model setup, but this cannot be judged from this short and confusing paragraph. The rest of the paragraph discusses how various parameters are determined for the model (tensile strength, Young's modulus), but the references are for bulk snow measurements, whereas it seems that a discrete model that explicitly simulates ice bonds should be using parameters for pure ice.*

Answer to comment m9). We completely agree that this section might be the one that has been misleading for the reviewer about the link between macroscopic (bulk) and contact (bond) properties and thus might need clarifications. This paragraph will be more detailed. We will add, as stated before more details about the mixed-mode shear-compression loading tests performed to obtain the failure envelope of the WL and we will add a figure describing it (Fig. 6 of the reply). However, we do not think that it is worth adding more details about the biaxial test protocol since it is a classic test which allows to obtain the macroscopic (bulk) properties of a material. In addition, to answer the last comment, we would have to use pure ice parameters for the grain if the snow was reconstructed directly from its microstructure, similarly to what Hagenmuller et al. (2015) did. In our case, as we work at a larger scale (see new paragraph in Appendix), we rather cared about getting the bulk properties correct.

Comment m10). *p 620, lines 20-22: the stress in a bending slab or beam depends on where within the beam you are interested. I understand from the context that you are interested in the maximum tensile stress at the tensile face of the beam, but you need to explicitly state this for the reader.*

Answer to comment m10). This will be stated more explicitly.

Comment m11). *p 629, 3rd paragraph: this is far too late in the paper to introduce the weak layer structure used in the model. This should come in the model description/setup, along with a justification for how and why you build the granular weak layer as you do.*

Answer to comment m11). The WL structure was already described in the "Formulation of the model" paragraph (p. 614, l. 14). However, the WL structure will be described in more detail as also suggested by reviewer # 1 by showing a zoom on the WL, instead of Fig. 4b (the contact will be describe more precisely by the new figure showing the contact model, see comment 3) by reviewer #1).

Comment m12). *p 630, line 2: if the analysis is preliminary and incomplete, then leave it out.*

Answer to comment m12). We remove "preliminary" and "still incomplete" as now our first results on the subject are quite clear. We prefer to leave this in the Discussion as it clearly informs the reader that the propagation speed we get from the simulations and the experiments is the propagation speed of the collapse wave but may be different from the "real" propagation speed. This is very important to consider for future research in this field.

Comment m13). *Table 2: it seems that a DEM setup should use ice parameters for strength and stiffness rather than bulk snow values, such that the bulk model setup should reproduce the bulk snow parameters. Putting in bulk snow values for the ice bonds and trusting the bulk response of the model seems like a backward approach. Finally, how can you specify the tensile strength of the weak layer (1.6 kPa to such precision? This seems arbitrarily precise. How sensitive is the model to this parameter?*

Answer to comment m13). As stated before and explained in our new paragraph (see the Appendix), we did not use either the bulk ice or the bulk snow parameters for the DEM setup (contact parameters). The contact parameters were calibrated to get the correct macroscopic parameters. This approach is commonly followed to model fracture of concrete (Hentz et al., 2004). In addition, as also stated before and as stated in the text, we performed mixed-mode shear-compression loading tests to get the failure envelope of the weak layer. To get the tensile strength, we performed a test for a loading angle of 180 degrees (pure tension test). However, there was a small misprint in the value of the WL tensile strength which is 0.6 kPa and not 1.6 kPa, as shown by the new figure (Fig. 6, tensile strength corresponding to the strength for a zero shear strength and a loading angle of 180 degrees). This global amplitude of the failure envelope was chosen such as that the WL did not fail in compression under the self weight of the slab $\rho g D \in [200 \text{ Pa}; 700 \text{ Pa}]$ (compressive strength = 750 Pa, see the

new figure of the failure envelope for a zero shear stress and a zero loading angle.) and that it allows crack propagation. This information will also be added to the paper to clarify this point. Concerning the sensitivity of the model to this parameter and more generally to the failure envelope, please see the last paragraph of the answer to comment 4) of reviewer #1.

Comment m14). *Table 3: which tensile strength is varied in the sensitivity analysis? Slab or weak layer, or both?*

Answer to comment m14). Thanks for this remark. This is the slab tensile strength. It will be added to the table caption.

Comment m15). *Figure 1: this figure has been published already many times. Are there not any other surface hoar pictures available?*

Answer to comment m15). This picture is the best we found to justify our simplified structure for the weak layer.

Comment m16). *Figure 3: this is for an actual PST measurement in the field? This is not clear from the caption. More descriptive detail is needed.*

Answer to comment m16). Thanks for this remark. We agree this was not clear. This is for the field PST. More details will be added to the caption.

Comment m17). *Figure 4: the contact bond model schematic needs explanation. What is A and B? Are you really using spheres of different size? If not, this is misleading. What is the shaded area, and the dashed lines?*

Answer to comment m17). This figure will be removed and replaced by a more detailed figure of the contact law as suggested by both reviewers. Instead, we will add a zoom on the weak layer structure.

Comment m18). *What are the properties of the foundation below the weak layer? A completely rigid foundation should lead to different response than a deformable foundation. This could also be explored in a sensitivity analysis, and might be revealing.*

Answer to comment m18). The substratum is completely rigid as clearly stated in section 2.2.2 line 10 as well as in the caption of Figure 4. We agree that it could also be interesting to study the effect of the elasticity of the substratum but we think - given the present breadth of our paper - this is beyond the scope. Furthermore, PST field measurement show (van Herwijnen et al., 2010) that the deformation is mainly located in the slab and in the WL. Almost no displacements were recorded in the substratum which justifies our assumption.

Comment m19). *Figure 12: what are the dashed vertical lines and tick marks in the panels? These are not labelled or explained, yet presumably they represent something...*

Answer to comment m19). Thanks for this remark. The dashed lines represent the position of the crack tip and the schematic of the crack represent the slab tensile failure. This will be added to the figure caption.

Appendix: new paragraph in section Motivation and objectives

The new parts of the paragraph are highlighted in blue.

(...) The latter processes are generally modeled under a continuum mechanics frame work, using methods such as finite elements (Podolskiy et al., 2013, and references therein). While these methods can be used to assess the stability of a layered snow cover, i.e. determine the conditions of failure occurrence and the onset of crack propagation, they are less suited to study what occurs after failure, i.e. during the dynamic phase of crack propagation, due to a lack in relevant constitutive models for the WL, including softening, and thus a [loss of objectivity with respect to the mesh in dynamic problems](#).

The objective of the proposed approach is to use the discrete element method (DE) to study the dynamic phase of crack propagation in a weak snowpack layer below a cohesive slab. The DE method is adequate for our purpose because: 1) no assumption is made about where and how a crack can be formed and propagate, and 2) the material is naturally discontinuous and well adapted to dynamic issues. We will show that, this method allows us to capture all the main physical processes involved in the release of dry slab avalanches, namely the complex mechanical behavior of the weak layer and the interplay between basal crack propagation, slab bending, and slab fracture. However, an important preliminary issue to address, concerns the scale of the considered model. In the weak layer, we intend to represent, through a simplified description, the particular collapsible and highly porous micro-structure of the snow in order to be able to reproduce the main features of the failure envelope of this material. As will be shown, we achieve this by using triangular-shaped elements of centimeter size. To account for the possible breakage of these elements, they consist of small cohesive grains of size r_{wl} . In the slab, on the contrary, due to computational costs, it would be completely unrealistic to try to account for the complete microstructure of the snow at the scale of a real slope or even at the scale of a field test such as the PST. The slab is thus modeled as a continuous material with an elastic-brittle constitutive behavior. Yet, similar to what is classically done for concrete (Meguro and Hakuno, 1989; Kusano et al., 1992; Camborde et al., 2000; Hentz et al., 2004), for instance, the response of this layer to the dynamic propagation of failure in the WL is also computed with the DE method. In that case, however, the considered elements (grains of size r) have no physical meaning and should only be regarded as entities of discretization similar to the mesh size in FE models. The contact parameters need to be properly calibrated (through classical biaxial tests, for instance) in order to recover the correct macroscopic properties of the material. Other continuous methods, such as FE, could have been used to simulate the slab, but - apart from avoiding the non-trivial issue of coupling DE and FE regions - the use of DE is well suited to represent the large deformations involved in the bending of the slab and the spontaneous formation of the tensile fracture.

To summarize, we contend that, unlike in other DE applications which are at the scale of the microstructure (e.g. Cundall (1989); Iwashita and Oda (2000) for frictional granular materials or Hagenmuller et al. (2015) for snow), the grains involved in the DE model developed in this study should not be regarded as snow grains, and that both r_{wl} and r are only discretization scales whose choice will result from a compromise between resolution and computational cost as classically done to model concrete fracture (Hentz et al., 2004). We consider here a meter-scale model where the advantage of the DE method is its ability to mimic the poorly-known mechanical response of the weak layer and to account for the different modes of failure displayed by snow (shear, compression, tension). The only microstructural scale directly accounted for is the size of the triangular elements in the weak layer, which are on the same order as the weak layer thickness, since it is a necessary ingredient for reproducing the particular mechanical behavior of this layer.

References

- Belytschko, T., H. Chen, J. Xu, and G. Zi, 2003: Dynamic crack propagation based on loss of hyperbolicity and a new discontinuous enrichment. *International Journal for Numerical Methods in Engineering*, **58**(12), 1873–1905.
- Bohren, C. F. and R. L. Beschta, 1974: Comment on wave propagation in snow. *American Journal of Physics*, **42**(1), 69–70.
- Camborde, F., C. Mariotti, and F. Donzé, 2000: Numerical study of rock and concrete behaviour by discrete element modelling. *Computers and geotechnics*, **27**(4), 225–247.
- Cambou, B. and M. Jean, 2001: Micromécanique des matériaux granulaires.
- Chandel, C., P. K. Srivastava, and P. Mahajan, 2015: Determination of failure envelope for faceted snow through numerical simulations. *Cold Regions Science and Technology*.
- Cundall, P. A., 1989: Numerical experiments on localization in frictional materials. *Ingenieur-archiv*, **59**(2), 148–159.

- Gaume, J., G. Chambon, I. Reiweger, A. van Herwijnen, and J. Schweizer, 2014: On the failure criterion of weak-snow layers using the discrete element method. *P. Haegeli (Editor), 2014 International Snow Science Workshop, Banff, Alberta.*
- Gaume, J., A. van Herwijnen, G. Chambon, and J. Schweizer, 2015: A simple analytical model to assess the critical length for crack propagation in weak snowpack layers derived from discrete element simulations. *Geophysical Research Abstracts*, **17**(EGU2015-11092).
- Gauthier, D. and B. Jamieson, 2006: Towards a field test for fracture propagation propensity in weak snowpack layers. *J. Glaciol.*, **52**(176), 164–168.
- Gauthier, D. and B. Jamieson, 2008: Evaluation of a prototype field test for fracture and failure propagation propensity in weak snowpack layers. *Cold Reg. Sci. Technol.*, **51**(2), 87–97.
- Hagenmuller, P., G. Chambon, and M. Naaim, 2015: Microstructure-based modeling of snow mechanics: a discrete element approach. *The Cryosphere Discussions*, **9**(1425-1460).
- Hamre, D., R. Simenhois, and K. Birkeland, 2014: Fracture speed of triggered avalanches. In *P. Haegeli (Editor), Proceedings ISSW 2014. International Snow Science Workshop, Banff, Alberta, Canada, 29 September - 3 October 2014*, 174-178.
- Hentz, S., F. V. Donzé, and L. Daudeville, 2004: Discrete element modelling of concrete submitted to dynamic loading at high strain rates. *Computers & structures*, **82**(29), 2509–2524.
- Hsieh, C. and C. Wang, 2004: The measurement of the crack propagation speed in rock slabs. In *Proceedings of the ISRM International Symposium 3rd ARMS*, Ohnishi and Aoki, editors, 341-346.
- Iwashita, K. and M. Oda, 2000: Micro-deformation mechanism of shear banding process based on modified distinct element method. *Powder Technology*, **109**(1), 192–205.
- Jamieson, B. and C. Johnston, 1990: In-situ tensile tests of snowpack layers. *J. Glaciol.*, **36**(122), 102–106.
- Johnson, B., J. Jamieson, and R. Stewart, 2004: Seismic measurements of fracture speed in a weak layer snowpack layer. *Cold Reg. Sci. Technol.*, **40**, 41–45.
- Kanninen, M., 1968: An estimate of the limiting speed of a propagating ductile crack. *Journal of the Mechanics and Physics of Solids*, **16**(4), 215–228.
- Kusano, N., T. Aoyagi, J. Aizawa, H. Ueno, H. Morikawa, and N. Kobayashi, 1992: Impulsive local damage analyses of concrete structure by the distinct element method. *Nuclear engineering and design*, **138**(1), 105–110.
- Lengliné, O., R. Toussaint, J. Schmittbuhl, J. E. Elkhoury, J. Ampuero, K. T. Tallakstad, S. Santucci, and K. J. Måløy, 2011: Average crack-front velocity during subcritical fracture propagation in a heterogeneous medium. *Physical Review E*, **84**(3), 036104.
- McClung, D., 1979: In situ estimates of the tensile strength of snow utilizing large sample sizes. *J. Glaciol.*, **22**(87), 321–329.
- McClung, D., 2005: Approximate estimates of fracture speeds for dry slab avalanches. *Geophysical Research Letters*, **32**(8).
- McClung, D., 2007: Dry snow slab shear fracture speeds. *Geophysical research letters*, **34**(10).
- Meguro, K. and M. Hakuno, 1989: Fracture analyses of concrete structures by the modified distinct element method. *Structural engineering/earthquake engineering*, **6**(2), 283–294.
- Reiweger, I., J. Gaume, and J. Schweizer, 2015: A new mixed-mode failure criterion for weak snowpack layers. *Geophys. Res. Lett.*, **42**.

- Scapozza, C., 2004: *Entwicklung eines dichte- und temperaturabhängigen Stoffgesetzes zur Beschreibung des visko-elastischen Verhaltens von Schnee*. PhD thesis, ETH Zürich.
- Sigrist, C., 2006: *Measurements of fracture mechanical properties of snow and application to dry snow slab avalanche release*. PhD thesis, ETH Zürich.
- Sigrist, C. and J. Schweizer, 2007: Critical energy release rates of weak snowpack layers determined in field experiments. *Geophys. Res. Lett.*, **34**(3).
- Song, J.-H., P. Areias, and T. Belytschko, 2006: A method for dynamic crack and shear band propagation with phantom nodes. *International Journal for Numerical Methods in Engineering*, **67**(6), 868–893.
- Truman, J. C., 1973: Wave propagation in snow. *American journal of physics*, **41**(2), 282–283.
- van Herwijnen, A. and B. Jamieson, 2005: High speed photography of fractures in weak snowpack layers. *Cold Reg. Sci. Technol.*, **43**(1-2), 71–82.
- van Herwijnen, A., J. Schweizer, and J. Heierli, 2010: Measurement of the deformation field associated with fracture propagation in weak snowpack layers. *J. Geophys. Res.*, **115**(F3).